Gloria Knolls Slide: a prominent submarine landslide complex on the Great Barrier Reef margin of north-eastern Australia

Graphical Abstract

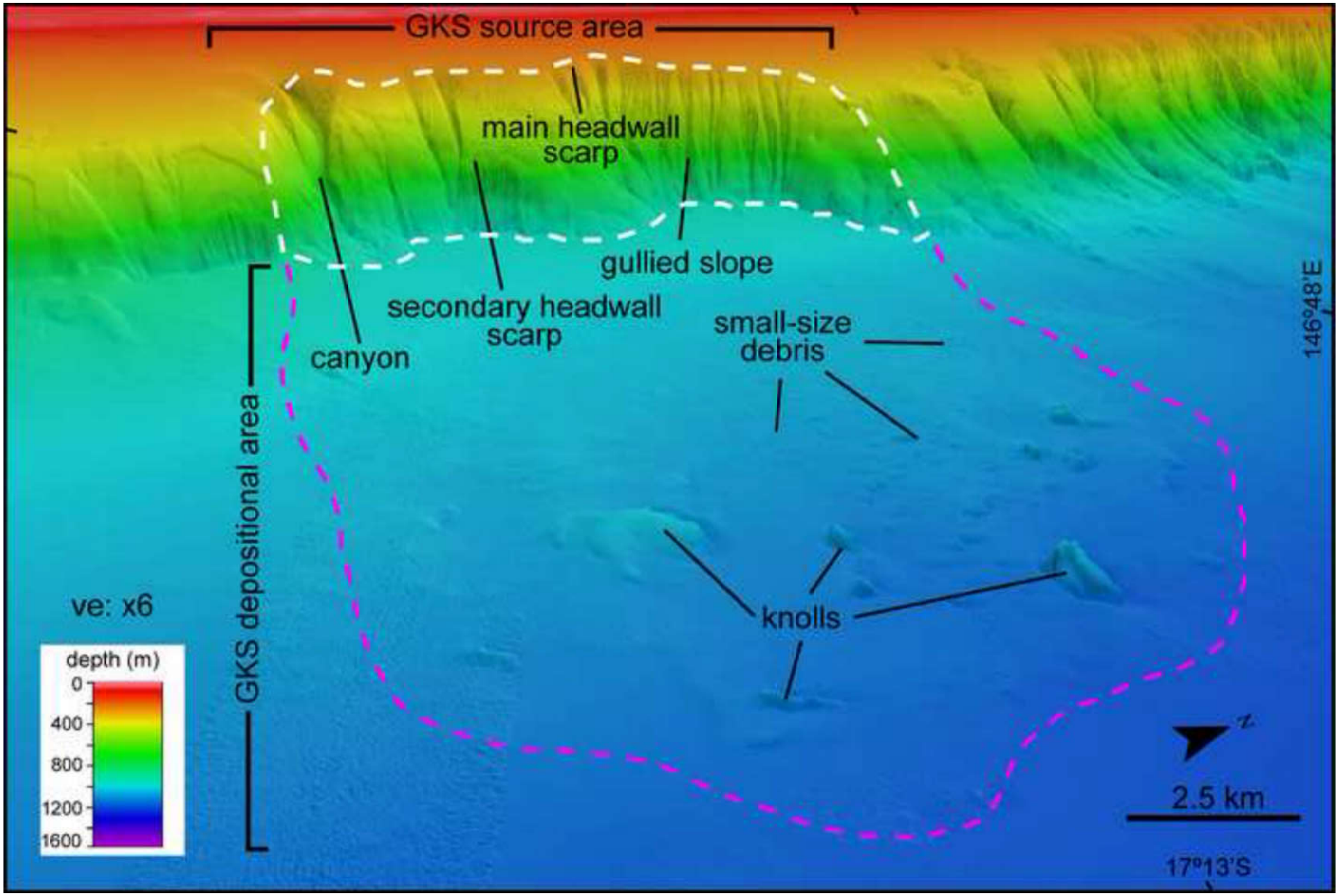

*Highlights (for review)

The GKS is the largest landslide complex on the Great Barrier Reef margin

Distinctive cluster of 8 knolls and over 70 small debris blocks in the distal area

The timing of emplacement of the GKS was at least before 302 ka

Failure process includes 3 events spreading from the lower slope to the upper slope

Cold-water coral community identified on the largest slide knolls

Gloria Knolls Slide: a prominent submarine landslide complex on the Great Barrier Reef margin of north-eastern Australia

Ángel Puga-Bernabéu [a,c], Robin J. Beaman [b], Jody M. Webster [c], Alex L. Thomas [d], Geraldine Jacobsen [e]

[a] Departamento de Estratigrafía y Paleontología, Universidad de Granada, 18002 Granada, Spain
[b] College of Science and Engineering, James Cook University, PO Box 6811, Cairns, QLD 4870, Australia
[c] Geocoastal Group, School of Geosciences, The University of Sydney, NSW 2006, Australia
[d] School of Geosciences, The University of Edinburgh, Edinburgh EH9 3FE, UK
[e] Institute for Environmental Research, Australia Nuclear Science and Technology Organisation, Locked Bag 2001, Kirrawee, NSW 2232, Australia

Abstract

We investigate the Gloria Knolls Slide (GKS) complex on the Great Barrier Reef margin of north-eastern Australia, the largest extant mixed carbonate-siliciclastic province in the world. Based on the most complete bathymetric and sub-bottom profile datasets available for the region, we describe the main surface and subsurface geomorphologic characteristics of this landslide complex. The GKS forms a 20 km along-slope and 8 km across-slope indentation in the margin, extending from 250 to 1350 m depth, and involves a volume of 32 km^3 of sediment remobilized during three events. Three main seafloor terrains can be distinguished based on seafloor morphology: a source area, a proximal depositional area and a distal depositional area. The source area includes a main headwall scarp with a maximum height of 830 m and a secondary scarp at 670 m depth. The proximal depositional area is flat and smooth, and lacks debris exposed on the seafloor. The distal depositional area has a hummocky surface showing a distinctive cluster of eight knolls and over 70 small debris blocks. A dredge sample from the top of the largest knoll at a depth of 1170 m reveals the presence of a cold-water coral community. In the sub-bottom profiles, the mass-transport deposits in the GKS are identified below the background sediment drape as partially confined, wedge-shaped bodies of mostly weak amplitude, transparent reflectors in the proximal

depositional area; and more discontinuous and chaotic in the distal depositional area. The failed sediment slabs of the GKS were evacuated, transported and disintegrated downslope in three events following a sequential failure process spreading successively from the lower slope to the upper slope. The first event initiated at the lower slope at the depth of the secondary scarp, moved downslope and disintegrated over the basin floor leaving coherent blocks. The subsequent second and third events were responsible for the formation upslope of the main scarp in the GKS. The timing of emplacement of the first GKS event, constrained by radiometric age of fossil biota from the surface of the largest slide block, was at least before 302±19 ka. The presence of alternating mixed carbonate and siliciclastic lithologies that build the slope might have played an important role as a preconditioning factor in this region. Preliminary estimations suggest that unusually large seismic events were the most likely triggering mechanism for the GKS. This work contributes to the understanding of large mass-movement deposits in mixed carbonate-siliciclastic margins and provides a useful morphologic characterization and evolutionary model for assessing its tsunamigenic potential with further numerical simulations. In addition, the discovery of a cold-water coral community on top of the largest knoll has implications for identifying similar landslide-origin cold-water coral communities on the GBR margin.

Keywords:
Continental slope; Slope failures; Mass transport deposits; Tsunamigenic potential; Cold-water coral; Great Barrier Reef

1. Introduction

Late Pleistocene and Holocene sedimentary records and numerical modelling suggest that submarine landslides have generated tsunami waves that might have reached significant heights at the coast (Bondevik et al., 1997, 2005; Fisher et al., 2005; Geist et al., 2009; Özeren et al., 2010; Iglesias et al., 2012). Landslide-generated tsunamis in recent times have created noticeable material damage and loss of lives, for example the 1979 Nice tsunami (Antibes city inundated, 8 fatalities; Assier-Rzadkieaicz et al., 2000; Sahal and Lemahieu, 2011), the 1998 Papua New Guinea tsunami (structures fully along the coast, over 2100 fatalities; McSaveney et al., 2000; Synolakis et al., 2002), and the 1929 Grand Banks tsunami (12 telegraph cables, 28 casualties; Fine et al., 2005). Therefore, although most submarine landslides are not tsunamigenic, their study has significant implications for assessing the potential natural hazards facing populated coastal areas.

Submarine landslides occur in different tectonic settings with many of them reported within the Quaternary. Glaciated margins host the largest landslides (10,000s km^2 and a few 1000s km^3) on Earth (Laberg and Vorren, 2000; Haflidason et al., 2004; Vanneste et al., 2006), together with those related to the collapse of the volcanic flanks from oceanic islands (Moore et al., 1989; Masson et al., 2002). In contrast, landslides on active tectonic margins are generally much smaller (10s to few 1000s km^2 and a few 10 km^3; Tappin et al., 2001; von Huene et al., 2004; Fisher et al., 2005; Harders et al., 2010; Strozyk et al., 2010) because the higher frequency of seafloor shaking by earthquakes in those settings. Earthquakes are one of the most important triggering mechanisms of slope failures (Locat and Lee, 2002; Masson et al., 2002) and it is suggested that frequent large earthquakes might limit the landslide volume on such active margins (Tappin et al., 2007; Völker et al., 2012). However, studies on submarine mass-wasting are relatively scarce on modern carbonate or mixed carbonate-siliciclastic passive margins (Hine et al., 2002; Puga-Bernabéu et al., 2013a; Principaud et al., 2015; Tournadour et al., 2015; Webster et al., 2016). Given that one of the preconditioning factors for landslide generation might be the presence of weak layers in the sedimentary succession (Haflidason et al., 2003; Laberg et al., 2003; Harders et al., 2010), it is important to note that the intrinsic characteristics of mixed carbonate-siliciclastic margins are the variable lithologies with different rheologic properties which vary spatially and temporally. Furthermore, recent studies have shown that submarine landslides might favour deep-water coral bank development by creating a suitable substratum where cold-water corals can settle on (De Mol et al., 2009; Savini et al., 2016).

In this study, we investigated the Great Barrier Reef (GBR) margin of north-eastern Australia, the largest extant mixed carbonate-siliciclastic province in the world (Davies et al., 1991a). Based initially on multibeam bathymetry along the GBR margin, we identified a large km-scale (20 km wide and 8 km across) indentation in the margin and the associated blocks and larger knolls found downslope at the toe of the slope, which are interpreted as a submarine landslide complex, herein called the Gloria Knolls Slide (GKS). We present the most comprehensive and high-resolution bathymetric and sub-bottom profile datasets available for the region, and describe the main surface and subsurface geomorphologic characteristics of the GKS. We then discuss the timing, possible pre-conditioning factors and triggering mechanisms, and compare the results with landslides generated in other tectonic settings. We also performed a simple first order estimation of the tsunamigenic potential of the GKS which, together with its morphologic characterization, provides useful information for more robust numerical simulations in the future aiming to assess the generation,

propagation and impact of potential tsunamis generated by the submarine landslides shaping this margin.

2. Regional setting

The north-eastern Australia margin is a passive continental margin that constitutes a large depositional area, from the shallow-water environment of the GBR shelf to the deeper slope and basin settings in the adjacent Queensland Trough (Fig. 1). The study area is located on the central part of this margin opposite the town of Innisfail. The shelf is a gently dipping surface, about 65 km wide, with the shelf-break located at 102 to 109 m depth (Abbey et al., 2011). The outer-shelf includes a series of submerged features, such as barrier reefs, lagoons, pinnacles and terraces (Abbey et al., 2011; Hinestrosa et al., 2016). The shelf is connected to a moderately steep (4° to 7°) continental slope. Regionally, the slope is excavated by a submarine canyon system perpendicular to the margin that extends to the base of the slope between about 900 to 1200 m, and deepens towards the north (Puga-Bernabéu et al., 2013b; Fig. 1A). The slope area studied in detail is located about 6 km south of Noggin Canyon 17 (Puga-Bernabéu et al., 2013b; Fig. 1B), and a potential landslide block called the "Noggin Block" found perched at the head of this canyon (Puga-Bernabéu et al., 2013a). The continental slope passes laterally to the basin floor of the Queensland Trough. The axis of this trough gently deepens towards the north with an average gradient <0.15° (Puga-Bernabéu et al., 2013b).

Modern surface sediments on the slope and in the basin comprise both terrigenous siliciclastics and biogenic carbonates with a variable spatial distribution along the margin (Dunbar et al., 2000; Francis et al., 2007). Subsurface slope sediments collected during ODP Leg 133 (Sites 819, 820 and 821; Fig. 1A) about 70 km north of the study area, revealed the presence of mixed carbonate-siliciclastic sediments since the Late Pleistocene at about 400 m below the seafloor (Davies et al., 1991). These deposits comprise couplets of clay-rich and carbonate-rich oozes that form fining upward, carbonate-decreasing sequences, and coarsening upward, carbonate-increasing sequences. These sequences are disrupted by mass movement deposits found throughout the cores (Davies et al., 1991a). In the deeper basin, long sediment cores (ODP Leg 133 Site 823; Fig. 1A) reveal the presence of interbedded hemipelagic muds, turbidites, debris flows and slump deposits since the Middle Miocene (Watts et al., 1993). Closer to the study site, short cores (FR4/92 PC12, PC16; Fig. 1A) record sediments varying between carbonate-rich and siliciclastic-rich intervals, and occasional thin turbidite layers (Dunbar et al., 2000; Page et al., 2003).

3. Material and methods

3.1. Multibeam data

During a 2007 RV *Southern Surveyor* voyage (Webster et al., 2008), a group of large knolls were located in the Queensland Trough, initially identified using GLORIA sidescan imagery (Hughes-Clarke, 1994) and hence called the Gloria Knolls, which showed up as clusters of high-reflectance pixels contrasting against a generally featureless area of the trough. A Kongsberg EM300 multibeam system was used to survey an area of approximately 20 km x 20 km over the site in depths of about 1100 to 1300 m. All bathymetry data were post-processed in Caris HIPS/SIPS software to remove any noise and adjust for sound velocity in the water column. The cleaned ASCII xyz (long, lat, depth) records were imported into ESRI raster grid files and QPS Fledermaus SD files as digital elevation models (DEMs) using a grid pixel size of 30 m. Another RV *Southern Surveyor* voyage in 2008 (Tilbrook and Matear, 2009) collected additional EM300 multibeam data along the GBR margin upslope of the knolls site and across a large scarp found on the continental slope (Fig. 1). These multibeam bathymetric datasets, plus all previously available bathymetry data for the GBR, were compiled to produce both 30 and 100 m DEMs for the study area (Beaman, 2010).

3.2. GIS analysis

The geomorphometric analysis included the calculation of slope gradient, maximum slope direction and surface curvature using ArcGIS Spatial Analyst tools on the 30 m and 100 m DEMs. The slope gradient was calculated for each pixel based on the elevation of its nearest neighbours in a 3 x 3 pixel window. Maximum slope direction (aspect) was classified into eight groups of values corresponding to the cardinal points. Plan curvature was calculated perpendicular to the direction of the maximum slope and allows the differentiation of ridges (positive values) and valleys (negative values). Profile curvature was calculated in the direction of the maximum slope, with positive values corresponding to upwardly concave surfaces and negative values to upwardly convex surfaces.

To understand the potential volume loss of the material removed from the GBR margin due to the GKS, a pre-slide continental slope 30 m DEM was developed in ArcGIS that followed the general gradients of the non-scarp slope area found to the north and south of the larger scarp feature. The ArcGIS Spatial Analyst Cut/Fill application was then used to calculate a net loss of slope by comparing the volume loss of the reconstructed initial surface against the observed scarp surface.

170

171 3.3 Sub-bottom profile data

172 During 2007 and 2008, a Kongsberg TOPAS PS-18 seismic system was used to acquire
173 shallow sub-bottom profiles from the outer-shelf, across the continental slope and into the
174 Queensland Trough. Several long transects were acquired over the Gloria Knolls themselves
175 in water depths of about 1200 to 1300 m. Two representative across and along sections over
176 the basin floor adjacent to the GKS headscarp and one section over the knolls site were
177 selected. The resulting SEG file profiles were viewed with the application DMNG SeiSee,
178 and representative gray-scale profiles were exported as bitmap images to manually draw
179 interpreted sub-bottom strata within Adobe Illustrator software. The Y axis units from the
180 profile were converted to depth in m, using TWT in ms and assuming a sound velocity of
181 1550 m s^{-1} (Davies et al., 1991a).

182

183 3.4. Rock dredge and sediment data

184 In 2007, a single rock dredge was taken across the crest of the largest knoll No. 1
185 (17°18.07'S, 146°56.10'E) in a depth of about 1170 m (see Fig. 1B for location). The chain
186 mesh bag was full and contained about 1 m^3 of sediment, which was first sorted by hand to
187 remove any semilithified and lithified nodules, fossil material and live biota, and then
188 thoroughly washed through a 1 cm sieve to retain any smaller samples. All live biota were
189 preserved in ethanol, and the fossil samples were dried and then stored for post-cruise age
190 dating and taxonomic identification.

191 Sedimentological analyses were conducted on the components of the sediment matrix,
192 which included: (1) carbon, nitrogen and sulfur (CNS) weight percent, and $CaCO_3$ weight
193 percent on three representative samples of soft mud, a semi-lithified nodule and a lithified
194 nodule; (2) Wentworth size classes using a Malvern laser particle sizer for the mud fraction
195 (<0.063 mm), sand fraction (0.063 to 2 mm) and gravel-fraction (>2 mm) as volume percent
196 on two samples of soft mud and semi-lithified nodules (i.e. excluded lithified nodules).
197 Sediment was classified following Folk (1954); and (3) XRD analyses of the carbonate,
198 quartz and clay weight percent on three samples of soft mud, semi-lithified nodule and
199 lithified nodule. Additionally, two thin section slides were taken of the lithified nodules to
200 ascertain if they had an internal structure, such as concentric concretions or pellets.

201

202 3.5. Age data

Age dating for this study comes from 13 ages provided by accelerator mass spectrometry (AMS) radiocarbon analysis of fossil samples conducted at the Australia Nuclear Science and Technology Organisation (ANSTO). In addition, sub-samples of three fossil scleractinian corals that were used for AMS dating were also analysed to provide three paired U-Th ages (yr BP; see Supplementary Material 1 for U-Th dating methods). The radiocarbon ages were calibrated using the Marine13 calibration curve (Reimer et al., 2013). It should be noted that this calibration curve is for surface waters (to a depth of 75 m) and as these corals are from deep waters, so these calibrations can only be approximations. Calibrations were performed using a local reservoir age, ΔR, which was determined from the U/Th age (representing the atmospheric ^{14}C age) and measured marine age from the same sample as described in detail by Russell et al. 2011 (Equation 1). The modelled marine age was obtained interpolating the measured atmospheric ^{14}C age against the Marine13 calibration curve. ΔR is then the difference between the measured ^{14}C marine age and the modelled marine age. The error for ΔR is calculated as shown in Equation 2 (Weisler et al. 2009).

$$\Delta R = \text{measured marine age} - \text{modelled marine age} \quad (1)$$

$$\sigma\Delta R = (\sigma \text{ measured age}^2 + \sigma \text{ modelled age}^2)^{0.5} \quad (2)$$

While three radiocarbon U-Th paired ages were determined, only one pair was suitable for the local reservoir age determination. The paired dates for OZL547 were not used as the ages are close to the ^{14}C background and the second pair of dates for OZL549 had a large error associated with the U-Th age. The modelled marine reservoir age for OZL548 was estimated by modelling in CALIB 7.1 (Stuiver et al. 2005) against the Marine13 curve, with $\Delta R = 0$. The modelled value of 1510±10 ^{14}C yrs BP gave a calibrated age range similar to the atmospheric age range determined by the U-Th dating (Weisler et al. 2009). Thus the local reservoir age was calculated from the paired U-Th age for OZL548 and gave a ΔR of 1,045±75 ^{14}C years BP.

This regional reservoir age was then used in the calibration of the radiocarbon ages, using the Marine13 dataset within CALIB 7.1 (Stuiver et al., 2005), with the results shown in Table 4.

4. Results

4.1. Seafloor morphology and structure of the Gloria Knolls Slide complex

The GKS source area and deposits are located between ~75 to 100 km offshore the coastal town of Innisfail, from 17º12.50'S to 17º25'S, and 146º41.75'E to 147º00'E (Fig. 1). The GKS excavated a ~174 km^2 area of the GBR margin slope at water depths from 250 to 1080 m, with slide debris extending out to 1350 m depth. The horizontal dimensions of the source area range from an along-slope distance of 20 km to about 8 km across-slope, forming a large re-entrant indentation of the slope at this location, about 7 km seaward from the shelf-edge and the reef-front (Figs. 1 and 2; Table 1A). Three main seafloor terrains can be distinguished based on seafloor morphology.

4.1.1. Source area and slide mass

The source area is located on the slope below 250 m depth and is formed by a main slide scar that marks the detachment of the upper slope, and a secondary scarp in deeper water (Figs. 1 and 2). The main headwall scarp has a bow shape and a maximum height of 830 m. The gradient in this scarp is much steeper (15-17º average) compared to the gradient of the reconstructed initial slope and the non-failure slope area lying to the north and south of the scarp (~6-7º; Fig. 3). The secondary scarp, similar in shape, is located in the southern part of the GKS at ~670 m depth, with a height of 400 m and an average gradient of 17º (Figs. 1, 2 and 3). The toe of the scarps displays two parts with an arcuate morphology in plan-view separated by a central area. This central area remained less affected after the slide, with gentler slope gradients (~8º; Fig. 3, profile 3). No tensional cracks or pockmarks are observed on the upper slope shoulder landward of the main headwall scarp. The source area is now carved by small <1 km wide and <100 m deep gullies in the northern part of the main headwall and a larger >2 km wide and >250 m deep, single canyon in the southern part (Fig. 1B). The gullies or canyons are oriented perpendicular to the direction of the main headwall scar and do not cut into the shelf. Lying north and south of the scarp at the foot of the slope are also small landslide scarps with cohesive debris zones lying close to the foot of the slope (Figs. 1B and 2F; Puga-Bernabéu et al., 2013b).

The cut/fill analysis and the comparison between pre- and post-failure slope cross sections yield a maximum thickness of the mass involved in the slide complex ranging from 260 to 500 m (south to north; Fig. 3), with an estimated net loss volume of 32 km^3 of slope sediment after the failure events.

4.1.2. Proximal depositional area (PDA)

The PDA extends over 10 to 14 km across the basin floor from the toe of the headwall scarp at depths between 1050 and 1200 m (Fig. 2A). The seafloor is flat and smooth, with gradients <1º both across and along the basin floor (Fig. 2B). No debris accumulation zone is obvious directly adjacent to the base of this scarp, although part of the evacuated sediment from the source area remains buried under hemipelagic sediment (see Section 4.2). The net downslope direction visible in the aspect map is to the east-northeast (Fig. 2C). The planar curvature map (Fig. 2D) shows subtle elongated, concave-up (negative curvature) features on the seafloor but there is no clear evidence of linear features suggesting glide tracks (e.g. Nissen et al., 1999).

4.1.3. Distal depositional area (DDA)

The DDA extends from about 1200 to 1350 m depth (Fig. 2A), and represents the main observed depocentre of the GKS. The seafloor evolves from relatively flat in the PDA to an uneven, hummocky surface in this area. Two depositional slide features are observed: large blocks (i.e. the knolls); and smaller debris blocks (Figs. 2 and 4).

The distinctive cluster of eight knolls covers an area over the surrounding seafloor of ca. 15.3 km^2 with the shortest distance between two adjacent knolls of 300 m and the longest distance of 3.4 km (Fig. 4; Table 2; Supplementary Material 2). The area of the largest knoll (No. 1) is about 7.9 km^2 with a height above the surrounding seafloor of 105 m and is ~3.6 km long. The smallest knoll in size (No. 4) is approximately 0.5 km^2 in area with a height of 63 m and is 900 m long. The knolls range in height from 179 m (No. 5) to 44 m (No. 2) above the surrounding seafloor. The knolls generally have rounded crests although several knolls (Nos. 2, 4) show ridge-like crest morphology. Their perimeter shapes vary from near-elliptical (Nos. 1, 3, 5) to more elongate shapes (Nos. 2, 4), with no obvious preferred orientation. Some knolls have additional ridges extending from the crests and down their sides (Nos. 1, 5, 8). All knolls show evidence of moats on their northern sides which excavate between about 12 to 44 m into the adjacent surrounding seafloor (Fig. 4). The maximum runout distance extends to about 30 km when measured from the top of the main headwall scarp to the furthermost knoll. This maximum runout distance could not be more accurately resolved by measuring the displacement of the failed sediment mass centre (Lastras et al., 2004b), as much of the sediment has subsequently been evacuated.

Also within the DDA, over 70 individual smaller debris blocks are distributed over an uneven, topographically irregular seafloor around the eight larger knolls, displaying a pattern of small elevated blocks separated by linear to sinuous depressions (Fig. 2E). The debris in

303 the northern part are nearly-circular, regularly spaced, small at 5 to 15 m high, and 300 to 500
304 m wide (Fig. 4). The gradients of the eastern side of the smaller debris blocks are steeper (3-
305 4º) than the western sides (<1º). Some of the smaller debris form arcuate ridges separated by
306 deeper depressions. In the southern part of the DDA, westwards from knoll No.1, debris are
307 larger and elongated in shape (Fig. 4).
308
309 4.2. Sub-bottom expression
310 The sub-bottom profiles across and along the basin floor over the GKS allowed us to
311 recognize different seismic reflection patterns in the proximal and distal depositional areas
312 identified on the seafloor bathymetry (Fig. 5).
313 At the toe of the slope, in the PDA, the uppermost strata form a relatively thin (~10 ms)
314 wedge-shaped body of chaotic to nearly transparent, low-amplitude reflectors occurring just
315 below the seafloor (Fig. 5A). This body shows small toe thrusts (Fig. 5A), and it corresponds
316 to a mass-transport deposit younger than those forming the GKS, which lies some metres
317 below. Seawards from this deposit, near-surface sediments consist of continuous parallel to
318 sub-parallel high amplitude reflectors bundled with low amplitude reflectors (Fig. 5B), which
319 correspond respectively to hemipelagic and sediment gravity flow (SGF) deposits. These
320 deposits represent the background sedimentation on this part of the basin (Dunbar et al., 2000;
321 Puga-Bernabéu et al., 2013a, 2014).
322 The internal character of the deeper deposits forming the GKS is different from the post-
323 failure strata described above. The mass-transport deposits in the GKS are identified below
324 the background drape as a partially confined, wedge-shaped bodies of mostly weak amplitude,
325 transparent reflectors in the PDA, and more discontinuous and chaotic in the DDA (Fig. 5A).
326 These bodies pinch out basinwards and laterally over about 20 km. In the PDA, some
327 continuous, high-amplitude sets of reflectors are intercalated between thick levels of
328 transparent reflectors (M1 and M2; Fig. 5B). A basal shear surface is not well observed in the
329 sub-bottom profiles but it presumably lies between 60 and 40 ms below the seafloor, forming
330 an irregular surface (Fig. 5B). The lateral boundaries of the slide are marked by onlap
331 terminations at the southern side and offset of the reflectors at the faulted northern side (Fig.
332 5B). Several blocks 300 to 400 m wide, characterized by nearly transparent reflection patterns
333 and rising from the adjacent reflectors, lie buried under the hemipelagic sediment drape in the
334 PDA (Fig. 5B). Towards the DDA, blocks of similar size crop out over the seafloor (Fig. 5A).
335 Within the DDA, discontinuous reflectors display imbricate or compressional patterns
336 forming small thrusts or pressure ridges at the toe of the slide (Fig. 5B). The total thickness of

the GKS deposits observed in the sub-bottom profiles parallel to the headwall ranges between 17 and 37 m (22 and 48 ms; Fig. 5B), with the thickest part in the southern half. In the downslope direction, the thickness varies from 31 to 23 m (about 30 to 40 ms; Fig. 5A).

The sub-bottom profile over four of the larger knolls (Nos. 1, 3, 7, 8; Fig. 5C) also shows other buried debris blocks, whose expression on the seafloor result in the uneven, irregular topography between the knolls (Figs. 2 and 4). The profile shows up to 26 m below seafloor of alternating strata, as opaque chaotic layers between parallel reflectors either side of the knolls, which correspond to the background basin fill sediments. The knolls themselves are relatively steep sided and the bulk of the blocks are acoustically opaque, but with up to 15 m of less distinct strata capping the knolls (e.g. No. 1; Fig. 5C). Moats can also be seen as notches in the seafloor on the northern sides of the knolls (Nos. 1, 3; Fig. 5C). The profile therefore shows evidence that the slope failure occurred first, and over time the resulting debris blocks were buried by alternating hemipelagic sediments and SGF deposits within the basin.

4.3. Sediment description and dating results

4.3.1. Sedimentology

The dredge sample from knoll No. 1 recovered a matrix of stiff, light brown-coloured mud, together with semi-lithified nodules and lithified nodules up to 15 cm in size. Many of the nodules were covered in a Fe-Mn oxide crust (Supplementary Fig. 1). We investigated the origin of the nodules to see if they were derived *in situ* from the soft mud sediment. The CNS analysis of the soft mud, semi-lithified nodules, and lithified nodules resulted in low nitrogen weights of 0.02 to 0.03%, and similar low sulphur weights of 0.03 to 0.04% (Table 3). There were small but noticeable increases in the carbon weights from the soft mud (6.56%) to semi-lithified (9.34%) to lithified nodules (10.55%), possibly due to an increasing proportion of $CaCO_3$ cement as the nodules become lithified. The soft mud and semi-lithified nodules showed mud fraction (<0.063 mm) volumes of 59.62% and 67.52% respectively, and sand fraction (0.063 to 2 mm) volumes of 40.38% and 32.48% respectively. There were no gravel fraction (>2 mm) volumes in these two samples. Both the soft mud and semi-lithified samples are defined as a sandy mud. The XRD data indicate little variation in the bulk calcium carbonate (78.1 to 83.5%), quartz (7.9 to 8.6%), and clay weights (7.8 to 13.6%) between the three sample types. Interestingly, the XRD results of the mud fraction and sand fraction splits from the soft mud and semi-lithified nodule reveal that the mud-sized components are dominated by siliciclastics, and the sand-sized components are dominated by carbonates.

Therefore, the finer grains have likely been derived from land, whereas the sand is possibly derived from hemipelagic/reefal carbonates. Additionally, the two thin sections taken from the lithified nodules revealed no concentric concretions or the presence of pellets to their internal structure.

4.3.2. Biota taxonomy

Interspersed within the sandy mud there was a remarkable variety of live and fossil biota (Supplementary Fig. 1). Many fossil samples had Fe-Mn oxide sub-millimetre crusts on their surfaces but there were also fossils that lacked any Fe-Mn staining. Samples of live biota consisted of broken gorgonian seawhips (possibly *Nicella* spp. and *Viminella* spp.) up to 15 cm long, and broken unidentified scleractinian corals with their bases still attached to the lithified nodules. Fossil samples were very common within the sediment matrix, and also showed a preference for coral bases to be attached to lithified nodules. The colonial scleractinian coral species identified were *Madrepora oculata*, *Enallopsammia rostrata*, and a fossil species of *Enallopsammia* which could not be identified as an extant coral and is possibly a new species (M. Kitahara personal communication). Solitary scleractinian corals from the Family Caryophylliidae and numerous pieces of bamboo coral from the Family Isididae were also found, either as disarticulated internodes or as broken branches up to 20 cm in length. Small gastropods of a few cm in size whose assemblages of species (*Gemmula* sp., *Leucosyrinx* sp., *Pontiothauma* sp., *Calliotropis pagodiformis*) have previously been found in about 1000 m of water off the North Island of New Zealand (B. Marshall personal communication). Other molluscs included pteropods, bivalves and unidentified scaphopods. Many loose plates of the stalked barnacle *Scillaelepas fosteri* were also scattered throughout the sediment matrix. This barnacle species is previously recorded from the New Zealand sub-Antarctic Islands (Newman, 1980), but this is the first record of that species from Australian waters (D. Jones personal communication).

4.3.3. Ages

The rock dredge likely excavated only the top 0.5 m of the seabed surface of the knoll and resulted in a random mixing of fossils (and therefore ages) for the individual samples. While not as ideal as a long sediment core that would preserve the sequence of ages in the core, it still provides a useful spread of ages to the fossil samples. The 13 uncalibrated ages range from 2.28±0.03 to 44.86±0.85 kyr BP (Table 4). The calibrated ages range from 0.78±0.14 to greater than 50,000 cal kyr BP (the radiocarbon age exceeded the limit for the Marine13

405 calibration curve). The three samples with paired U-Th analyses have ages of:
406 301,899±19,105 (OZL547); 1,066±34 (OZL548); and 914±306 (OZL549) yr BP. The old age
407 (301,899±19,105 kyr BP) from the U-Th analysis suggests that the two oldest radiocarbon
408 ages of about 45 kyr BP, likely represent background ages older than about 50 kyr BP, and
409 are radiocarbon-dead. Interestingly, one of these older samples is possibly an undescribed
410 (non-extant) species of *Enallopsammia*, while the other is a lithified nodule. Taken together,
411 these data reveal a spread of ages ranging from at least 302 kyr BP till modern times.
412
413 **5. Discussion**
414 **5.1. Evolution of the slope failure**
415 The failed sediment slabs of the GKS were evacuated, transported and disintegrated
416 downslope forming a suite of relatively well-preserved blocks embedded within a loose
417 matrix over the seafloor (e.g. Laberg and Vorren, 2000; Canals et al., 2004; Hogan et al.,
418 2013; Figs. 4 and 5). In the case of the GKS, the relatively flat seafloor adjacent to the toe of
419 the scarp and the absence of coherent blocks, extensional ridges and/or other deformation
420 structures at this proximal location (Gardner et al., 1999; Lastras et al., 2006; Hogan et al.,
421 2013) point to a complete evacuation of the collapsed material. The presence of slope gullies
422 excavated into the headwall scarp and the lack of hanging terraces in the headwall area, also
423 support this fact. The available data suggest that sediment evacuation did not occur in a single
424 event but likely as a result of several events formed by retrogressive sliding. The presence of
425 a secondary scarp in the southern part of the GKS (Fig. 2) can be considered an evidence of
426 multi-phase instability (Canals et al., 2004; Twichell et al., 2009). Sub-bottom seismic
427 profiles show the presence of at least two chaotic mass-transport deposits separated by
428 hemipelagic sediments (Fig. 5B). Collapsed blocks, however, rise from deeper positions
429 within the sediment cover (Fig. 5A, B), and thus they were presumably emplaced before the
430 first mass-transport deposit shown in Figure 5B.
431 Based on the morphometric analysis of the bathymetry data combined with cross-sectional
432 sub-bottom profiles, we interpret that the present-day expression of the GKS resulted from a
433 sequential failure process spreading successively from the lower slope to the upper slope (Fig.
434 6). Under an external trigger mechanism (see Section 5.3), sediment destabilization initiated
435 at the lower slope, likely at water depths of the secondary headwall scarp, moved downslope
436 and disintegrated over the basin floor leaving some coherent debris (Event 1), some of which
437 were prominent enough to remain above the seafloor during subsequent burial phases (Fig. 5).
438 Sub-bottom profiles do not allow us to discern whether compressive structures formed at the

distal part of the landslide. Although variable, the orientation of the long axes of some large blocks is perpendicular to the transport direction which may result from compression (Huvenne et al., 2002). The removal of large amounts of sediments in this first stage could therefore lead to an increase in slope angle, favouring subsequent slope instabilities. The following collapse (Event 2) involved the emplacement of the first large mass-transport deposit (M1 in Fig. 5B), which moved over the seafloor passing through the previous debris and infilling the irregular surface left behind by the earlier event. Disintegrated material reached the distal area and was locally subject to compression, likely due to the presence of the hummocky surface, forming small thrusts or pressure ridges (Figs. 5A and 6). This second event was followed by a period of hemipelagic deposition and intercalated SGF (debrites and turbidites; Event 3) as shown in the sub-bottom profiles (Fig. 5B), suggesting that dismantling of the slope did not stop completely. These later deposits were progressively smoothing the seafloor surface. The third event is represented by another large mass-transport deposit (M2 in Fig. 5B) which was emplaced similarly to the second event, including the formation of pressure ridges. Although we cannot accurately determine this from available data, we hypothesize the following links between the mass-transport deposits M1 and M2 of events 2 and 3 and their source areas. Due to the larger size of the mass-transport deposit M1 compared with M2 (Fig. 5B), the event 2 was linked to the formation of the main GKS scarp. Additionally, event 3 might be related to a re-shaping of the remaining slope. Post-failure hemipelagic sedimentation progressively buried the landslide deposits, and canyons and gullies began at the failed slope. At more recent times, smaller landslides events, likely related to canyon and gully activity, were deposited at the toe of the GKS scarp (Figs. 5A and 6).

While the inception and evolutionary model proposed for the GKS could be improved by additional sub-bottom data, it is consistent with the morphologic features observed on the adjacent seafloor to the south and north of the headwall. Here, the lower slope is dissected by a more or less continuous set of smaller landslides whose scarps are located at similar depths to that of the secondary GKS scarp (~670 m; Figs. 1B and 2). This may suggest that this part of the slope is prone to collapse under specific triggering mechanisms. Furthermore, the upper slope is affected by incipient sliding (Puga-Bernabéu et al., 2013a) which could be a smaller-scale analogue of the second GKS event.

5.2. Timing

On passive margins such as north-eastern Australia, the timing of slope failures is thought to be related to sea-level variations, especially during glacial times and transition to interglacial periods (Owen et al., 2007; Lee, 2009: Webster et al., 2016). However, at the global scale, there is no significant statistical correlation of landslide frequency with sea-level changes (Urlaub et al., 2013). We have constrained the timing of the first GKS event by using the radiometric age of fossil biota recovered from the surface of the largest slide block, which provides a minimum age of emplacement. The oldest sample dated in this study (302±19 kyr BP, Table 4) are from a surface dredge, hence older material lying deeper within the sediment were not sampled. However, the ~14 to 15 m of sediment strata capping the knolls provide an additional constraint on the emplacement age. Two nearby sediment cores, FR4/92 PC12 and FR4/92 PC16 (Fig. 1A) yielded overall sedimentation rates of 0.034 and 0.09 m kyr^{-1} (derived from age models based on correlation of sediment properties to SPECMAP; Dunbar et al., 2000). The sedimentation rate on top of the knolls is likely to be lower due to their elevated positions and the effect of increased current velocities. This effect can been seen in the thickness of the sediment package covering knoll No. 7, which is approximately half as much as the adjacent sediment from the surrounding seafloor (Fig. 5). The FR4/92 sediment cores therefore provide a maximum constraint on the sedimentation rate on the knolls. For ~14 to 15 m to accumulate at a rate of 0.034 m kyr^{-1}, the knolls must have been in place for likely 412 to 441 kyr BP. Taken together, these constraints suggest the emplacement of the large knolls (event 1) likely occurred during the transition from Marine Isotopic Stage 12 to 11, when the amplitude of the sea-level change was the largest in the last million years (Lisiecki and Raymo, 2005; Rohling et al., 2014). The timing for the subsequent younger slide events (see Section 5.1) cannot be assessed with the available data.

5.3. Triggering mechanisms and pre-conditioning factors.

The triggering mechanisms for submarine landslides include different processes which may act together to reduce the shear strength and lead to sediment mass failure downslope. The most important triggers include high sedimentation rates and overpressure, ocean waves, gas hydrate dissociation and seismic activity (Bea et al., 1983; Piper et al., 1999; Matsumoto et al., 2003; Sultan et al., 2003, 2004a; Lafuerza et al., 2012; Crutchley et al., 2016).

High sedimentation rates may trigger slope failures by creating high excess pore pressures in the sediment and/or by oversteepening (Baraza et al., 1990; Wolinsky and Pratson, 2007; Dugan and Sheahan, 2012). These high rates are related to environmental factors such as sea-level change and sediment input. It is widely accepted that during sea-level lowstands, large

amounts of terrigenous sediments are transported to the deep ocean basins which could favour rapid sediment deposition (Posamentier and Vail, 1998; Posamentier and Erksin, 1991; Carvajal and Steel, 2006; Normark et al., 2006). However, this is not the case for the GBR margin, where the maximum rates of sediment supply to the slopes occurred during the late transgression (Dunbar et al., 2000; Page et al., 2003). In the central GBR, many upper slope landslides have been identified nearby a large deltaic system (paleo-Burdekin River lying ~150 km to the south-east; Webster et al., 2016). However, the GKS study area lacks any large deltaic or fluvial systems similar to the paleo-Burdekin River that may provide large amounts of sediment to the slope. Sedimentation rates on the GBR uppermost slope, between 200 and 300 m depth, are relatively low to moderate, from 20 to 50 cm ky^{-1} (Dunbar et al., 2000). Therefore, it seems unlikely that high sedimentation rates alone can account for the inception of the GKS.

Ocean waves, such as storm waves and tsunamis can generate cyclically oscillating high- and low-pressure on the seafloor sediments, and in some cases have the potential to generate slope failures (Sterling and Strohbeck, 1975; Bea et al., 1983; Rogers and Goodbred Jr., 2010; Casalbore et al., 2012). The GBR margin is affected periodically by tropical cyclones (Puotinen, 2004), and some of them pass right across the study area as in the case of the Cyclone Yasi (Category 5) on the 3rd of February 2011 (Great Barrier Reef Marine Park Authority, 2011; Perry et al., 2014). However, both the secondary and the main headwall scarps of the GKS lies too deep (between 250 and 670 m depth) to be affected by direct cyclone pumping even during sea-level low-stands.

Gas hydrate dissociation may influence the static stable sediment conditions on the slope and lead to slope failures by modifying the sediment strength (Carpenter, 1981; Kayen and Lee, 1991; Sultan et al., 2004c). Theoretically, gas hydrates may form at the depth of the secondary headwall scarp of the GKS (670 m) and the gas hydrate stable zone may extend about 100 m below the seafloor (based on Kvenvolden, 1988 and Ruppel, 2007). However, no definitive gas hydrates have so far been identified in Australian waters (Geoscience Australia and BREE, 2012). The contribution of gas hydrate dissociation to slope failure in the study area cannot be evaluated with the available information, but its impact as a trigger cannot be dismissed and requires further research.

Earthquakes are one of the most effective external processes for triggering slope failures (Tappin et al., 2001; Fine et al., 2005). Although the GBR margin is a passive margin, recent seismic events of small magnitude (mostly M_w 2-4, up to M_w 5) have occurred within a radius of 150 km around the GKS location (Earth Systems Science Computational Centre, 2015;

Geoscience Australia, 2015). Slope stability simulations show that the margin slope in nearby (<10 km) areas is stable under current static gravitational loading, but it may collapse under a seismic event yielding a peak horizontal acceleration of 0.2-0.4 g (Puga-Bernabéu et al., 2013a). This horizontal acceleration can be generated at short hypocentral distances and short periods by large M_w 7.0 earthquakes, which is consistent with the maximum earthquake magnitude estimated elsewhere in Australia (MW 7. 0-7.5±0.2, Allen et al. 2011). The seismic events might have a local source associated with the N-NW regional faults that affect the basement and overlying sediments nearby the study area (Symonds et al., 1983). Therefore, a unusually large seismic event could have acted as possible triggering mechanism for the first event of the GKS.

Earthquake shaking, although an important trigger, probably represents the final push for landslide generation, and thus pre-conditioning or susceptibility factors have also to be taken into account. The presence of weak layers in the slope sedimentary successions favour slope instabilities, as these beds can show different mechanical behaviour compared with the surrounding sediment (Haflidason et al., 2003; Kvalstad et al., 2005). Weak layers can form continuous horizons that may act as the slip plane for several slope failures. For example, in the Eivissa Channel (western Mediterranean), the contact between hydro-mechanical properties at the boundary between fine-grained sediments overlying methane-charge, relatively coarse deposits acted as a failure surface for at least four slides (the Ana, Joan, Nuna and Jersi slides; Lastras et al., 2004b, 2006; Lafuerza et al., 2012). In the GKS study area, no long sediment cores are directly available to assess the presence of weak layers. However, seismic lines and long cores from the Ocean Drilling Program Leg 133 across a slope transect (~70 km north of GKS, sites 819 through 821; Fig. 1A), provide useful information about the sub-bottom stratigraphy of the margin. Sediments from these cores record abundant Late Pleistocene multimetre-scale, coarsening-upward cycles with varying proportions of carbonates and siliciclastics, from clay-rich sediments with numerous silt intercalations to carbonate-rich bioclastic wackestones (Glenn et al., 1993). Interestingly, the presence of a slump appears with strong amplitude mounded reflectors at the top of the progradational seismic sequence 6 in site 819 (Davies et al., 1991b). The detachment surface of this slump occurred at the top of one of the coarsening upward cycles, and the depth below seafloor (~200 mbsf; Davies et al., 1991b) is similar to the depth of the secondary headwall scarp of the GKS below the reconstructed pre-failure seafloor (profiles 4 and 5 in Fig. 3). We suggest that the presence of alternating carbonate and siliciclastic lithologies, deposited during successive sea-level cycles at different sedimentation rates on this mixed margin,

might have generated weak layers within the sediment package. Rapid sea-level changes, such as during the MIS 12 to 11 transition when the first event of the GKS likely occurred, may have also contributed to the slope failure due to rapid sediment building during deglacial periods and transient excess pore pressures (Owen et al., 2007; Smith et al., 2013). Future research could focus on obtaining long sediment cores and subsurface geophysical information to better understand the pre-conditioning factors for mass-transport deposits in this archetypical mixed carbonate-siliciclastic margin.

5.4. Comparison with other submarine landslides

The GKS is the largest landslide complex discovered so far on the north-eastern Australia margin (Puga-Bernabéu et al., 2016), but asdetailed knowledge of other slope failures is virtually lacking on modern mixed carbonate-siliciclastic margins, we must compare this slide against other settings. In terms of sediment composition, the most direct comparison is with slope failures on the carbonate slopes of the Great Bahama Bank (GBB), the Little Bahama Bank (LBB) and the Exmouth Plateau of north-western Australia (Scarselli et al., 2013; Jo et al., 2015; Tournadour et al., 2015; Principaud et al., 2015). Large landslides on these margins are similar in terms of size and morphology to the GKS. These landslides have semicircular to box shapes, range from 10 to 23 km in length, 5 to 12 km in width, and remobilized about 15 to 30 km^3 of eroded slope sediments. The maximum size of collapsed coherent blocks remaining on the seafloor is also similar (about 2 km long). However, runout distances are variable, from very short (1.2 km) to about 20 km (Jo et al., 2015; Principaud et al., 2015) similar to the GKS. A significant difference with the GKS is the local development of slope fan systems fed by channelized flows linked to slumps in the Exmouth Plateau (Scarselli et al., 2013). The similar dimensions and characteristics of these landslides and the GKS might indicate comparable physical properties of sediment in the pre-failed slope and initiation processes. Landslide triggering mechanisms along the GBB and LBB margins include tectonic activity and high sedimentation rates, while seismic loading and fluid venting are the likely triggers along the Exmouth Plateau. However, as in the case of the GKS, these triggers remain unproven and need further constraint.

On passive siliciclastic margins, submarine landslides are generally more numerous and cover larger areas on the seafloor where the margin has been supplied by large river systems or glaciers (Twichell et al., 2009). The GKS is not a large landslide compared with the giant slope failures found in glaciated (or formerly) passive margins such as the Storegga Slide (Haflidason et al., 2004), the Hinlopen Slide (Vanneste et al., 2006) or the Trænadjupet Slide

(Laberg and Vorren, 2000), although it is comparable in size to some large landslides in river-fed passive margins (Canals et al., 2004; Lastras et al., 2002, 2004a; Ramprasad et al., 2011). High sedimentation rates, which are able to generate excess pore pressure in the sediment, likely influence the distribution of landslides in these margin types, particularly in the case of glacially-influenced slopes (Laberg and Vorren, 2000; Solheim et al., 2005). On the north-eastern Australia margin, sedimentation rates are low (see Section 5.3), and the controls and timing on sedimentation rates differ from those in passive siliciclastic margins (Dunbar et al., 2000; Dunbar and Dickens, 2003; Page et al., 2003) where they are driven by climate change between glacial and interglacial conditions. Equally important seems to be the presence of weak layers within the sedimentary succession, which are commonly linked to contourite layers intercalated within hemipelagic deposits in the case of glaciated margins (Solheim et al., 2005), or shelf-edge delta deposits and related bedding planes in the case of river-influenced margins (Prior et al., 1986). However, the possible interaction between landslides and contour currents (e.g. Krastel et al., 2011) remains uncertain in the GKS study area. As in most cases on passive margin slopes, the GKS is interpreted to be formed as a retrogressive slope failure, although the failed material is now fully evacuated. Passive margins far from the influence of continental glaciers, including the north-eastern Australia margin, are overall stable under present-day normal gravitational conditions (Baraza et al., 1990; Sultan et al., 2004b; Urgeles et al., 2006; Puga-Bernabéu et al., 2013a), and thus landslide initiation usually requires an external trigger, like a large earthquake.

The physiographic setting (shelf, slope, relatively shallow base-of-slope and basin), the dimensions (e.g. headwall scar length, volume of remobilized sediment) and the characteristics of the landslide areas defined for the GKS (source area, PDA and DDA) are similar to the latest Pleistocene BIG'95 slide (debris flow) in the western Mediterranean (Lastras et al., 2002, 2004a). Therefore, the comparison of similar seafloor expression, kinematic indicators and sedimentary features distributed along the different landslides domains (e.g. BIG'95 debris flow) may help to identify common patterns in the sediment failure process. The BIG'95 debris flow was the result of several processes involving materials with contrasting rheologies and specific source areas that led to deposition of a suite of cohesive blocks in an intermediate depositional area and a debrite, formed by more mobile material, in a distal depositional area up to 110 km far from the source area (Lastras et al., 2002, 2004a). Numerical simulations suggest that the highly mobile sediment mass pushed, sheared and accelerated in its movement downslope slabs of coherent sediments and continued flowing downslope once the block eventually stopped, although the effect

hydroplaning cannot be discarded (Lastras et al., 2005). The knolls and debris distribution in the DDA of the GKS is comparable to that of the blocks and block clusters in the BIG'95 debris flow, as well as the runout distance for such blocks (15-25 km). In contrast, apart from the disintegrated sediment surrounding the blocks, we have not identified slide sediments deposited out of the DDA in the GKS. We cannot discard the presence of such deposits as they might have been transported further downslope, now lying buried within the Queensland Trough (Fig. 1A), which may represent an analogue of the Valencia Channel in the case of the BIG'95 debris flow (Lastras et al., 2002, 2004a).

5.5. Tsunamigenic potential

The GKS is a relatively modest in size submarine landslide complex (Canals et al., 2004; Hühnerbach et al., 2004) but its dimensions, extending over 528 km^2 on the seafloor and remobilizing about 32 km^3 of sediment, is large enough to be considered as a potential tsunamigenic landslide, as has been suggested for landslides of similar size (McAdoo et al., 2000; ten Brink et al., 2006; Iglesias et al., 2012). The speed of the slide mass represents a key requirement in the assessment of tsunami potential and the height of the resulting tsunami wave can be only estimated on the basis of numerical hydrodynamic modelling of each particular landslide (Todorovska et al., 2002; Trifunac et al., 2002; Puzrin et al., 2010). Although, the detailed 3D numerical modelling of the potential tsunami linked to the GKS is out of the scope of the present study, a simple, first order approach is possible if we consider the basic morphometric parameters quantified here. Assuming the simplest case, a translational slide with no basal friction and strong fluid dynamic drag (Grill et al., 2009 and references therein), the maximum three-dimensional tsunami amplitude (η_o) is given by:

$$\eta_o = S_o\,(0.0574 - 0.0431\ \sin\theta)\left(\frac{T}{b}\right)\left(\frac{b\sin\theta}{d}\right)^{1.25}\left(1 - e^{-2.2(s-1)}\right)\left(\frac{w}{w+\lambda o}\right) \qquad (1)$$

where S_o is the distance of motion for translational failures,

$$S_o = \frac{\pi}{2}\,b(s+1) \qquad (2)$$

θ is the angle of the slope, T is the maximum thickness of the failed mass, b is the length of the slide mass, d the average depth above the center of the slide mass, s is the sediment specific gravity, w the slide mass width, and λ the tsunami wavelength,

$$\lambda_o = \sqrt{\frac{\pi b d (s+1)^2}{2\sin\theta(s-1)}} \qquad (3)$$

These numerical equations are valid within a range of $\theta \in [5, 30^{o}]$, $d/b \in [0.06, 1.5]$, $T/b \in [0.008, 0.2]$, and $s \in [1.46, 2.93]$ which are satisfied by the morphometric values calculated for the GKS.

The most conservative scenario is to consider a first large margin collapse at the depth of the secondary headwall scarp (Fig. 2), corresponding to the first event (Fig. 6). According to the predictive equations above, the sudden mass failure of this portion of the margin would yielda three-dimensional tsunami wave elevation of about 27 m. These waves are about three times greater than those modelled for the potential collapse of a small block ("Noggin Block" ~0.86 km^3) found on the upper slope 6 km north from the GKS (Puga-Bernabéu et al., 2013a). Run-up heights at the adjacent coast would depend on the sea-level position, the overall physiography of the margin, the period, size and direction of the incoming waves, beach morphology, bottom friction, and other parameters. It has also been suggested that the presence of the shelf reefs, if in existence at the time (Webster and Davies, 2003), would decrease tsunami amplitudes at the coastline to half or less (Baba et al., 2007; Webster et al., 2016). For example, the impact of a modelled 2 m high tsunami wave generated by a small-scale landslide (~0.025 km^3) in the southern central GBR, would have reached the coast with a height of 0.5 m (Webster et al., 2016). Nonetheless, a tsunami caused by the collapse of GKS would have been significant even if dampened by shelf reefs. This simple approach highlights the potential tsunami hazard of submarine landslides to the north-eastern Australia coast and thus the need for better characterization of slope failure processes on this margin.

5.6. Discovery of cold-water coral community

The discovery of a variety of both live and abundant fossil biota from the top of one knoll points to a cold-water coral community existing since at least 302 ka to modern times (Table 4 and Supplementary Fig. 1). The presence of three extant scleractinian coral species (and possibly one undescribed non-extant species), to bamboo corals, gorgonians, stalked barnacles, and various molluscs highlights a habitat that supports a cold-water coral community. The knolls appear to meet the geomorphic and environmental requirements for cold-water corals to settle and grow: (1) a suitable substratum of semi-lithified and lithified nodules as the necessary hard surface to attach to by providing a stable anchorage in a dynamic environment; and (2) food availability through locally accelerated currents over the knolls (De Mol et al., 2009). The eight knolls, up to 179 m in height above the surrounding seafloor, are likely to locally accelerate currents for enhanced food supply. Further, the moat

features on the northern sides of the knolls provide evidence for north-flowing currents sweeping over the knolls, thereby scouring any sediment on the leeward side bases. Such accelerated currents would also help to reduce sedimentation on the uppermost knoll surfaces where cold-water corals may grow, another requirement for the presence of corals (De Mol et al., 2009). The water mass at this depth is indicative of Antarctic Intermediate Water (AAIW; Solokov and Rintoul, 2000; Hartin et al., 2011) found below 700 to 1000 m. AAIW enter the Queensland Trough from the south and flows northwards towards the Coral Sea Basin (Solokov and Rintoul 2000) and is likely responsible for the scouring of moats around the knolls.

The existence of a cold-water coral community in the Queensland Trough provides a further example of the spatial relationship existing between submarine landslides and the presence of cold-water corals in the deep-sea (Viana et al., 1998; Huvenne et al., 2003; De Mol et al., 2009; Correa et al., 2011, Savini et al., 2016). Elsewhere along the GBR margin in depths to ~2000 m, we have identified smaller clusters of knolls, some up to 50 m high, near other landslide features derived from the lower slope (Puga-Bernabéu et al., 2011). It would be important to confirm if other blocks also have cold-water corals, as their environmental conditions are similar. Indeed, the depth of collection at the Gloria Knolls (1170 m) for the colonial scleractinia *Madrepora oculata* and *Enallopsammia rostrata*, conform to the depth ranges of these same species previously sampled off Queensland in the Coral Sea (Cairns, 2004). These species lie within a tropical province of azooxanthellate scleractinian corals that forms a subcluster of faunas with similarities to the Indo-Pacific seamounts and New Zealand (Cairns, 2004). This current work, and future research, will provide important baseline information for marine managers to assess the deep Great Barrier Reef and Coral Sea biodiversity in relation to seabed topography and oceanographic processes.

6. Conclusions

The GKS is the largest submarine landslide complex discovered so far on the Great Barrier Reef margin of north-eastern Australia. This slope failure removed 174 km^2 and remobilized about 32 km^3 of slope sediments during three mass-wasting events, leaving a steep headwall scarp up to 830 m in height, now shaped by younger gullies and a canyon. The dimensions of the GKS are within the range of submarine landslides in river-fed passive margins and carbonate-dominated margins.

The main depocentre of the GKS is located in the distal part of the slide, where a distinctive cluster of km-scale knolls and over 70 smaller debris blocks extend over an

743 irregular seafloor surface. The GKS deposits show weak amplitude, transparent reflectors in
744 the proximal depositional area and more discontinuous and chaotic in the distal depositional
745 area. In contrast, post-failure strata consist of continuous parallel to sub-parallel high
746 amplitude reflectors bundled with low amplitude reflectors.
747 The present-day expression of the GKS resulted from a sequential failure process
748 spreading successively from the lower slope to the upper slope. The GKS initiation was
749 probably the result of several processes involving varying carbonate and siliciclastic
750 lithologies in the region, favoured by a rapid relative sea-level rise, and most likely triggered
751 by an unusually large seismic event. The cold-water coral community identified on one of the
752 knolls provides important baseline information for marine managers to assess deep Great
753 Barrier Reef and Coral Sea biodiversity.
754
755
756 **Acknowledgments**
757 We thank the Captains and crew of the RV *Southern Surveyor* for their assistance during the
758 SS072007 and SS092008 expeditions, and the support of the staff at Australia's Marine
759 National Facility (http://www.marine.csiro.au/nationalfacility/). The 2007 voyage was also
760 funded by the National Geographic Society and the European Consortium for Ocean Research
761 Drilling. We thank Raphael Wust for the sediment analyses. The authors would like to thank
762 the Australian Research Council (DP1094001) for support and the Australia Institute of
763 Nuclear Science and Engineering for financial assistance (Award No. AINGRA09006) to
764 enable the AMS work on the fossil samples to be conducted. APB was also funded by the
765 Research Group RNM-190 of the Junta de Andalucía (Spain). We also thank two anonymous
766 reviewers for their constructive reviews.
767
768 **References**
769 Abbey, E., Webster, J.M., Beaman, R.J., 2011. Geomorphology of submerged reefs on the
770 shelf edge of the Great Barrier Reef: The influence of oscillating Pleistocene sea-levels.
771 Marine Geology 288, 61–78.

772 Allen, T.I., Burdidge, D.R., Clark, D., McPherson, A.A., Collins, C.D.N., Leonard, M., 2011.
773 Development of the next generation Australian National Earthquake Hazard Map. In:
774 Proceedings of the ninth pacific conference on earthquake engineering, building and
775 earthquake-resilient society, Auckland, New Zealand, paper 207, p. 8.

776 Assier-Rzadkieaicz, S., Heinrich, P., Sabatier, P.C., Savoye, B., Bourillet, J.F., 2000.
777 Numerical modeling of a landslide-generated tsunami: The 1979 Nice event. Pure and
778 Applied Geophysics 157, 1707–1727.

779 Baba, T., Mleczko, R., Burbidge, D., Cummins, P., Thio, H.K., 2007. The Effect of the Great
780 Barrier Reef on the Propagation of the 2007 Solomon Islands Tsunami Recorded in
781 Northeastern Australia. Pure and Applied Geophysics 165, 2003–2018.

782 Baraza, J., Lee, H.J., Kayen, R.E., Hampton, M.A., 1990. Geotechnical characteristics and
783 slope stability on the Ebro margin, western Mediterranean. Marine Geology 90, 379–393.

784 Bea, R.G., Wright, S.G., Sircar, P., Niedoroda, A.W., 1983. Wave-induced slides in South
785 Pass Block 70, Mississippi Delta. Journal of Geotechnical Engineering 109, 619–644.

786 Beaman, R.J., 2010. 3DGBR. A high-resolution depth model for the Great Barrier Reef and
787 Coral Sea. Marine and Tropical Sciences Research Facility (MTSRF) Project 2.5i.1a Final
788 Report. MTSRF (12 pp. Data available at: http://www.deepreef.org/bathymetry/65-3dgbr-
789 bathy.html).

790 Bondevik, S., Svendsen, J.I., Mangerud, J. 1997. Tsunami sedimentary facies deposited by the
791 Storegga tsunami in shallow marine basins and coastal lakes, western Norway.
792 Sedimentology 44, 1115–1131.

793 Bondevik, S., Lovholt, F., Harbitz, C.B., Mangerud, J., Dawson, A.G., Svendsen, J.I. 2005
794 The Storegga slide tsunami—comparing field observations with numerical simulations.
795 Marine and Petroleum Geology 22, 195–208. Cairns, S.D., 2004. The Azooxanthellate
796 Scleractinia (Coelenterata: Anthozoa) of Australia. Records of the Australian Museum 56,
797 259–329.

798 Canals, M., Lastras, G., Urgeles, R., Casamor, J.L., Mienert, J., Cattaneo, A., De Batist, M.,
799 Haflidason, H., Imbo, Y., Laberg, J.S., Locat, J., Long, D., Longva, O., Masson, D.G.,
800 Sultan, N., Trincardi, F., Bryn, P., 2004. Slope failure dynamics and impacts from seafloor
801 and shallow sub-seafloor geophysical data: case studies from the COSTA project. Marine
802 Geology 213, 9–72.

803 Carpenter, G., 1981. Coincident sediment slump/clathrate complexes on the U.S. Atlantic
804 continental slope. Geo-Marine Letters 1, 29–32.

805 Carvajal, R., Steel, R.J., 2006. Thick turbidite successions from supply-dominated shelves
806 during sea-level highstand. Geology 34, 665–668.

807 Casalbore, D., Bosman, A., Chiocci, F.L., 2012. Study of Recent Small-Scale Landslides in
808 Geologically Active Marine Areas Through Repeated Multibeam Surveys: Examples from
809 the Southern Italy. In: Yamada, T., Kawamura, K., Ikehara, K., Ogawa, Y., Urgeles, R.,
810 Mosher, D., Chaytor, J., Strasser (Eds.), Submarine mass movements and their
811 consequences, 5th International Sysmposium, pp. 573–582.

812 Correa, T.B.S., Grasmueck, M., Eberli, G.P., Reed, J.K., Verwer, K., Purkis, S., 2011.
813 Variability of cold-water coral mounds in a high sediment input and tidal current regime,
814 Straits of Florida. Sedimentology 59, 1278–1304.

815 Crutchley, G., Mountjoy, J.J., Pecher, I.A., Gorman, A.R., Henrys, S.A., 2016. with Shallow
816 Gas Hydrate Systems: Insights from New Zealand Examples. In: Lamarche, G., Mountjoy,
817 J., Bull, S., Hubble, T., Krastel, S., Lane, E., Micallef, A., Moscardelli, L., Mueller, C.,
818 Pecher, I., Woelz, S. (Eds.), Submarine mass movements and their consequences,
819 Advances in Natural and Technological Hazards Research 41, 401–410.

820 Davies, P.J., McKenzie, J.A., Palmer-Julson, A., et al., 1991a. Proceedings of the Ocean
821 Drilling Program Initial Reports 133. Ocean Drilling Program, College Station, TX.

822 Davies, P.J., McKenzie, J.A., Palmer-Julson, A., et al., 1991b. Proceedings of the Ocean
823 Drilling Program Initial Reports 133, Site 819. Ocean Drilling Program, College Station,
824 TX, pp. 451–508.

825 De Mol, B., Van Rensbergen, P., Pillen, S., Van Herreweghe, K., Van Rooij, D., McDonnell,
826 A., Huvenne, V., Ivanov, M., Swennen, R., Henriet, J.P., 2002. Large deep-water coral
827 banks in the Porcupine Basin, southwest of Ireland. Marine Geology 188, 193–231.

828 De Mol, B., Huvenne, V., Canals, M., 2009. Cold-water coral banks and submarine
829 landslides: a review. International Journal of Earth Sciences 98, 885–899.

830 Dugan, B., T.C. Sheahan. 2012. Offshore sediment overpressures of passive margins:
831 Mechanisms, measurement, and models. Reviews of Geophysics 50, RG3001,
832 http://dx.doi.org/10.1029/2011RG000379.

833 Dunbar, G.B., Dickens, G.R., 2003. Massive siliciclastic discharge to slopes of the Great
834 Barrier Reef Platform during sea-level transgression: constraints from sediment cores
835 between 15ºS and 16ºS latitude and possible explanations. Sedimentary Geology 162, 141–
836 158.

837 Dunbar, G.B., Dickens, G.R., Carter, R.M., 2000. Sediment flux across the Great Barrier Reef
838 Shelf to the Queensland Trough over the last 300 ky. Sedimentary Geology 133, 49–92.

839 Earth Systems Science Computational Centre (2011) University of Queensland. Queensland
840 earthquake map, Cairns region. http://www.quakes.uq.edu.au. Accessed 15 July 2015.

841 Fine, I.V., Rabinovich, A.B., Borhhold, B.D., Thomson, R.E., Kulikov, E.A., 2005. The
842 Grand Banks landslide-generated tsunami of November 18, 1929: preliminary analysis and
843 numerical modeling. Marine Geology 215, 45–57.

844 Fisher, M.A., Normark, W.R., Greene, H.G., Lee, H.L., Sliter, R.W., 2005. Geology and
845 tsunamigenic potential of submarine landslides in Santa Barbara Channel, Southern
846 California. Marine Geology 224, 1–22.

Folk, R.T., 1954. The distinction between grain size and mineral composition in sedimentary-rock nomenclature. Journal of Geology 62, 334–359.

Francis, J.M., Dunbar, G.B., Dickens, G.R., Sutherland, I.A., Droxler, A.W., 2007. Siliciclastic sediment across the North Queensland margin (Australia): A Holocene perspective on reciprocal versus coeval deposition in tropical mixed siliciclastic-carbonate systems. Journal of Sedimentary Research 77, 572–586.

Gardner, J.V., Prior, D., B., Field, M.E., 1999. Humboldt Slide - a large shear-dominated retrogressive slope failure. Marine Geology 154, 323–338.

Geoscience Australia, BREE, 2012. Australian Gas Resource Assessment 2012, Canberra, 68 p.

Geoscience Australia (2012) Earthquake Database. http://www.ga.gov.au/earthquakes/searchQuake.do; accessed December 2016.

Glenn, C.R., Kroon, D., Wei, W., 1993. Sedimentary rhythms and climatic forcing of Pleistocene-Holocene mixed carbonate/siliciclastic sediments off the Great Barrier Reef. In: McKenzie, J.A., Davies, PJ., Palmer-Julson, A., et al., 1993. Proceedings of the Ocean Drilling Program Scientific Results 133. Ocean Drilling Program, College Station, TX., pp. 189–202.

Grilli, S.T., Oliver-Denzil, S.T., Baxter, D.P., Maretzki, S., 2009. A probabilistic approach for determining submarine landslide tsunami hazard along the upper east coast of the United States. Marine Geology 264, 74–97.

Great Barrier Reef Marine Park Authority, 2011. Impacts of tropical cyclone Yasi on the Great Barrier Reef: a report on the findings of a rapid ecological impact assessment, GBRMPA, Townsville.

Haflidason, H., Sejrup, H.P., Berstad, I.M., Nygard, A., Richter, T., Lien, R., Berg, K., 2003. A weak layer feature on the northern Storegga slide escarpment. In: Miener, J., Weaver, P.P.E. (Eds), European margin sediment dynamics, pp. 55–62, Springer.

Haflidason, H., Sejrup, H.P., Nygard, A., Mienert, J., Bryn, P., Lien, R., Forsberg, C.F., Berg, K., Masson, D., 2004. The Storegga Slide: architecture, geometry and slide development. Marine Geology 213, 201–234.

Harders, R., Kutterolf, S., Hensen, C., Moerz, T., Brueckmann, W., 2010. Tephra layers: A controlling factor on submarine translational sliding? Geochemistry, Geophysics, Geosystems 11, Q05S23, doi:10.1029/2009GC002844

Harders, R., Ranero, C., Weinrebe, W., Behrmann, J.H., 2011. Submarine slope failures along the convergent continental margin of the Middle America Trench. Geochemistry, Geophysics, Geosystems 12, Q05S32, doi:10.1029/2010GC003401

Hartin C.A., Fine R.A., Sloyan B.M., Talley L.D., Chereskin T.K., Happell J., 2011. Formation rates of Subantarctic mode water and Antarctic intermediate water within the South Pacific. Deep-Sea Research I 58, 524–534.

Hine, A. C., Locker, S. D., Tedesco, L. P., Mullins, H. T., Hallock, P., Belknap, D. F., Gonzales, J. L., Neuman, A. C., Snyder, S. W., 1992, Megabreccia shedding from modern, low-relief carbonate platforms, Nicaraguan Rise. Geological Society of America Bulletin 104, 928–943.

Hinestrosa, G., Webster, J. M., and Beaman, R., 2016. Postglacial sediment deposition along a mixed carbonate-siliciclastic margin: new constraints from the drowned shelf-edge reefs of the Great Barrier Reef, Australia. Palaeogeography Palaeoclimatology Palaeoecology 446, 168–185.

Hogan, K.A., Dowdeswell, J.A., Mienert, J., 2013. New insights into slide processes and seafloor geology revealed by side-scan imagery of the massive Hinlopen Slide, Arctic Ocean margin. Geo-Marine Letters 33, 325–343.

Hughes-Clarke, J., 1994. Toward remote seafloor classification using the angular response of acoustic backscattering: a case study from multiple overlapping GLORIA data. IEEE Journal of Ocean Engineering 19, 364–374.

Hühnerbach, V., Masson, D.G., partners of the COSTA-Project, 2004. Landslides in the North Atlantic and its adjacent seas: an analysis of their morphology, setting and behavior. Marine Geology 213, 343–362.

Huvenne, V.A.I., Croker-Peter, F., Henriet, J.P., 2002. A refreshing 3D view of an ancient sediment collapse and slope failure. Terra Nova 14, 33–40.

Huvenne, V.A.I., De Mol, B., Henriet, J.-P., 2003. A 3D seismic study of the morphology and spatial distribution of buried coral banks in the Porcupine Basin, SW of Ireland. Marine Geology 198, 5–25.

Huvenne, V.A.I., Van Rooij, D., DeMol, B., Thierens, M., O'Donnell, R., Foubert, A., 2009. Sediment dynamics and palaeo-environmental context at keystages in the Challenger cold-water coral mound formation: Clues from sediment deposits at the mound base. Deep-Sea Research I 56, 2263–2280.

Iglesias, O., Lastras, G., Canals, M., Olabarrieta, M., González, M., Aniel-Quiroga, I., Otero, L., Durán, R., Amblas, D., Casamor, J.L., Tahchi, E., Tinti, S., De Mol, B., 2012. The BIG'95 Submarine Landslide–Generated Tsunami: A Numerical Simulation. The Journal of Geology 120, 31–48.

Jo, A., Eberli, G.P., Grasmueck, M., 2015. Margin collapse and slope failure along southwestern Great Bahama Bank. Sedimentary Geology 317, 43–52.

Kayen RE, Lee HJ (1991) Pleistocene slope instability of gas hydrate-laden sediment on the Beaufort Sea margin. Marine Geotechnology 10,125–141.

919 Kvenvolden, K. A. 1988. Methane hydrate—a major reservoir of carbon in the shallow
920 geosphere? Chemical Geology 71, 41–51.

921 Krastel, S., Wefer, G., Hanebuth, T.J.J., Antobreh, A.A., Freudenthal, T., Preu, B., Schwenk,
922 T., Strasser, M., Violante, R., Winkelmann, D., M78/3 shipboard scientific party, 2011.
923 Sediment dynamics and geohazards off Uruguay and the de la Plata River region (northern
924 Argentina and Uruguay). Geo-Marine Letters 31, 271–283.

925 Kvalstad, T.J., Andresen, L., Forsberg, C.F., Berg, K., Bryn, P., Wangen, M., 2005. The
926 Storegga slide: evaluation of triggering sources and slide mechanics. Marine and
927 Petroleum Geology 22, 245–256.

928 Laberg, J.S., Vorren, T.O., 2000. The Trænadjupet Slide, offshore Norway, morphology,
929 evacuation and triggering mechanisms. Marine Geology 171, 95–114.

930 Laberg, J.S., Vorren, T.O., Mienert, J., Haflidason, H., Bryn, P., Lien, R., 2003. Preconditions
931 leading to the Holocene Traenadjupet slide, offshore Norway. In: Locat, J., Mienert, J.
932 (Eds), Submarine mass movements and their consequences, pp. 247–254, Kluwer
933 Academic Publishers.

934 Lafuerza, S., Sultan, N., Canals, M., Lastras, G., Cattaneo, A., Frigola, J., Costa, S., Berndt,
935 C., 2012. Failure mechanisms of Ana Slide from geotechnical evidence, Eivissa Channel,
936 Western Mediterranean Sea. Marine Geology 307-310, 1–21.

937 Lastras, G., Canals, M., Hughes-Clarke, J.E., Moreno, A., DeBatist, M., Masson, D.G.,
938 Cochonat, P., 2002. Seafloor imagery from the BIG'95 debris flow, western
939 Mediterranean. Geology 30, 871–874.

940 Lastras, G., Canals, M., Urgeles, R., De Batist, M., Calafat, A.M., Casamar, J.L., 2004a.
941 Characterisation of a recent debris flow deposit on the Ebro margin, Western
942 Mediterranean Sea, after a variety of seismic reflection data. Marine Geology 231, 235–
943 255.Lastras, G., Canals, M., Urgeles, R., Hughes-Clarke, J.E., Acosta, J., 2004b. Shallow
944 slides and pockmark swarms in the Eivissa Channel, western Mediterranean Sea.
945 Sedimentology 51, 1–14.

946 Lastras, G., De Blasio, F.V., Canals, M., ElverhØi, 2005. Conceptual and numerical
947 modelling of the BIG'95 debris flow, western Mediterranean Sea. Journal of Sedimentary
948 Research 75, 784–797.

949 Lastras, G., Canals, M., Amblas, D., Ivanov, M., Dennielou, B., Droz, L., Akhmetzhanov, A.,
950 TTR-14 Leg 3 Shipboard Scientific Party, 2006. Eivissa slides, western Mediterranean
951 Sea: morphology and processes. Geo-Marine Letters 26, 225–233.

952 Lee, H.J., 2009. Timing of occurrence of large submarine landslides on the Atlantic Ocean
953 margin. Marine Geology 264, 53–64.

954 Lisiecki, L.E., Raymo, M.E., 2005. A Pliocene-Pleistocene stack of 57 globally distributed
955 benthic $\delta^{18}O$ records. Paleoceanography 20, PA1003. doi:10.1029/2004PA001071

956 Locat, J., Lee, H.J., 2002. Submarine Landslides: Advances and Challenges. Canadian
957 Geotechnical Journal 39, 193–212.

958 Masson, D.G., Watts, A.B., Gee, M.J.R., Urgeles, R., Mitchell, N.C., Le Bas, T.P., Canals,
959 M., 2002. Slope failures on the flanks of the western Canary Islands.

960 Matsumoto, T., Tappin, D.R., and SOS Onboard Scientific Party, 2003. Possible Coseismic
961 Large-scale Landslide off the Northern Coast of Papua New Guinea in July 1998:
962 Geophysical and Geological Results from SOS Cruises. Pure and Applied Geophysics 160,
963 1923–1943.McSaveney, M.J., Goff, J.R., Darby, D.J., Goldsmith, P., Barnett, A., Elliot, S.,
964 Nongkas, M. 2000. The 17 July 1998 tsunami, Papua New Guinea: evidence and initial
965 interpretation. Marine Geology 170, 81–92.

966 Mienis, F., van der Land, C., de Stigter, H.C., van de Vorstenbosch, M., de Haas, H., Richter,
967 T., van Weering, T.C.E., 2009. Sediment accumulation on a cold-water carbonate mound
968 at the Southwest Rockall Trough margin. Marine Geology 265, 40–50.

969 Moore, J.G., Clague, D.A., Holcomb, R.T., Lipman, P.W., Normark, W.R., Torresan, M.E.,
970 1989. Prodigious submarine landslides on the Hawaiian Ridge. Journal of Geophysical
971 Research 94, B12, 17465–17484.

972 Nissen, S.E., Haskell, N.L., Steiner, C.T., Coterill, K.L., 1999. Debris flow outrunner blocks,
973 glide tracks, and pressure ridges identified on the Nigerian continental slope using 3-D
974 seismic coherency. The Leading Edge 18, 595–599.

975 Normark, W.R., Piper, D.J.W., Sliter, R., 2006. Sea-level and tectonic control of middle to
976 late Pleistocene turbidite systems in Santa Monica Basin, offshore California.
977 Sedimentology 53, 867–897.

978 Owen, M., Day, S., Maslin, M., 2007. Late Pleistocene submarine mass movements:
979 occurrence and causes. Quaternary Science Reviews 26, 958–978.

980 Özeren, M.S., Çağatay, N., Postacıoğlu, N., Şengör, A.M.C., Görür, N., Eriş, K., 2010.
981 Mathematical modelling of a potential tsunami associated with a late glacial submarine
982 landslide in the Sea of Marmara. Geo-Marine Letters 30, 523–539.

983 Page, M.C., Dickens, G.R., Dunbar, G.B., 2003. Tropical view of Quaternary sequence
984 stratigraphy: siliciclastic accumulation on slopes east of the Great Barrier Reef since the
985 Last Glacial Maximum. Geology 31, 1013–1016.

986 Perry, C.T., Smithers, S.G., Kench, P.S., Pears, B., 2014. Impacts of Cyclone Yasi on
987 nearshore, terrigenous sediment-dominated reefs of the central Great Barrier Reef,
988 Australia. Geomorphology 222, 92–105.

989 Piper, D.J.W., Cochonat, P., Morrison, M., 1999. The sequence of events around the epicentre
990 of the 1929 Grand Banks earthquake: Initiation of debris flows and turbidity currents
991 inferred from sidescan sonar. Sedimentology 46, 79–97.

992 Posamentier, H.W., Vail, P.R.,1988. Eustatic control on clastic deposition II – sequence and
993 system tracts models. In: Wilgus, C.K., Hastings, B.S., Posamentier, H., Van Wagoner, J.,
994 Ross, C.A., Kendall, C.G.St.C. (Eds.), Sea Level Changes: an Integrated Approach, SEPM
995 Special Publication 42, pp. 125–154.

996 Posamentier, H.W., Erksine, R.D., 1991. Seismic expression and recognition criteria of
997 submarine fans. In: Weimer, P., Link, M.H. (Eds.), Seismic facies and sedimentary
998 processes of submarine fans and turbidite systems, New York, Springer-Verlag, pp. 197–
999 222.

1000 Principaud, M., Mulder, T., Hervé Gillet, Borgomano, J., 2015. Large-scale carbonate
1001 submarine mass-wasting along the northwestern slope of the Great Bahama Bank
1002 (Bahamas): Morphology, architecture, and mechanisms. Sedimentary Geology 317, 27–42.

1003 Prior, D.B., Doyle, E.H., Neurauter, T., 1986. The Currituck Slide, Mid-Atlantic continental
1004 slope–revisited. Marine Geology 73, 25–45.

1005 Puga-Bernabéu, Á., Webster, J.M., Beaman, R.J., Guilbaud, V., 2011. Morphology and
1006 controls on the evolution of a mixed carbonate-siliciclastic submarine canyon system,
1007 Great Barrier Reef margin, north-eastern Australia. Marine Geology 289, 100–116.

1008 Puga-Bernabéu, Á., Webster, J.M., Beaman, R.J., 2013a. Potential collapse of the upper slope
1009 and tsunami generation on the Great Barrier Reef margin, north-eastern Australia. Natural
1010 Hazards 66, 557–575.

1011 Puga-Bernabéu, Á., Webster, J.M., Beaman, R.J., Guilbaud, V., 2013b. Variation in canyon
1012 morphology on the Great Barrier Reef margin, north-eastern Australia: the influence of
1013 slope and barrier reefs. Geomorphology 191, 35–50.

1014 Puga-Bernabéu, Á., Webster, J.M., Beaman, R.J., Reimer, P.J., Renema, W., 2014. Filling the
1015 gap: A 60 ky record of mixed carbonate-siliciclastic turbidite deposition from the Great
1016 Barrier Reef. Marine and Petroleum Geology 50, 40–50.

1017 Puga-Bernabéu, Á., López-Cabrera, F.J., Webster, J.M., Beaman, R.J., 2016. Submarine
1018 landslides on the Great Barrier Reef margin, north-eastern Australia: Preliminary
1019 characterization of their morphology and behaviour. 35th International Geological
1020 Congress, 27th August-2nd September 2016, Cape Town, South Africa.

1021 Puotinen, M., 2004. Mapping tropical cyclone disturbance of the Great Barrier Reef. The
1022 Globe 55, 31–41.

1023 Puzrin, A.M., Saurer, E., Germanovich, L.N., 2010. A dynamic solution of the shear band
1024 propagation in submerged landslides. Granular Matter 12, 253–265.

1025 Ramprasad, T., Dewangan, P., Ramana, M.V., Mazumdar, A., Karisiddaiah, S.M., Ramya,
1026 E.R., Sriram, G., 2011. Evidence of slumping/sliding in Krishnae–Godavari offshore basin
1027 due to gas/fluid movements Marine and Petroleum Geology 28, 1806–1816.

Reimer, P.J., Bard, E., Bayliss, A., Beck, J.W., Blackwell, P.G., Ramsey, C.B., Buck, C.E., Cheng, H., Edwards, R.L., Friedrich, M., Grootes, P.M., Guilderson, T.P., Haflidason, H., Hajdas, I., Hatte, C., Heaton, T.J., Hoffmann, D.L., Hogg, A.G., Hughen, K.A., Kaiser, K.F., Kromer, B., Manning, S.W., Niu, M., Reimer, R.W., Richards, D.A., Scott, E.M., Southon, J.R., Staff, R.A., Turney, C.S.M., van der Plicht, J., 2013. INTCAL13 and MARINE13 radiocarbon age calibration curves 0-50,000 years cal bp. Radiocarbon 55, 1869–1887.

Rogers, K.G., Goodbred Jr, S.L., 2010. Mass failures associated with the passage of a large tropical cyclone over the Swatch of No Ground submarine canyon (Bay of Bengal). Geology 38, 1051–1054.

Rohling, E.J., Foster, G.L., Grant, K.M., Marino, G., Roberts, A.P., Tamisiea, E., Williams, F., 2014. Sea-level and deep-sea-temperature variability over the past 5.3 million years. Nature 508, 477–482.

Ruppel, C., 2007. Tapping methane hydrates for unconventional natural gas. Elements 3, 193–199, DOI: 10.2113/gselements.3.3.193.

Russell, N., Cook, G.T., Ascough, P.L. Scott, E.M. Dugmore, A.J., 2011. Examining the inherent variability in ΔR: New methods of presenting ΔR values and implications for MRE studies. Radiocarbon, 53, 277–288.

Sahal, A., Lemahieu, A., 2011. The 1979 Nice airport tsunami: mapping of the flood in Antibes. Natural Hazards 56 (3), 833–840.

Savini, A., Marchese, F., Verdicchio, G., Vertino, A., 2016. Submarine Slide Topography and the Distribution of Vulnerable Marine Ecosystems: A Case Study in the Ionian Sea (Eastern Mediterranean). In: Lamarche, G., Mountjoy, J., Bull, S., Hubble, T., Krastel, S., Lane, E., Micallef, A., Moscardelli, L., Mueller, C., Pecher, I., Woelz, S. (Eds.), Submarine mass movements and their consequences, Advances in Natural and Technological Hazards Research 41, 163–170.

Scarselli, N., McClay, K., Elders, C., 2013. Submarine Slide and Slump Complexes, Exmouth Plateau, NW Shelf of Australia. The Sedimentary Basins of Western Australia IV: Proceedings of the Petroleum Exploration Society of Australia Symposium, Perth, WA, 2013, pp. 1–20.

Smith, D.E., Harrison, S., Jordan, T., 2013. Sea-level rise and submarine mass failures on open continental margins. Quaternary Science Reviews 82, 93–103. In: Keep, M., Moss, S.J. (Eds), 2013, The Sedimentary Basins of Western Australia IV: Proceedings of the Petroleum Exploration Society of Australia Symposium, Perth, WA, 2013.

Solheim, A., Berg, K., Forsberg, C.F., Bryn, P., 2005. The Storegga Slide complex: repetitive large scale sliding with similar cause and development. The Storegga Slide complex: repetitive large scale sliding with similar cause and development. Marine and Petroleum Geology 22, 97–107.

1066 Solokov S., Rintoul S.R., 2000. Circulation and water masses of the Southwest Pacific:
1067 WOCE Section P11, Papua New Guinea to Tasmania. Journal of Marine Research 58,
1068 223–268.

1069 Sterling, G.H., Strohbeck, G.E.. 1975. The Failure of South Pass 70B Platform in Hurricane
1070 Camille, J. Petroleum Technology, March 263–268.

1071 Strozyk, F., Strasser, M., Strasser, M., Krastel, S., Meyer, M., Huhn, K., 2010. Reconstruction
1072 of retreating mass wasting in response to progressive slope steepening of the northeastern
1073 Cretan margin, eastern Mediterranean Marine Geology 271, 44–54.

1074 Stuiver, M., Reimer, P. J., Reimer, R. W. 2005. CALIB 5.0 (program and documentation
1075 available at http://calib.qub.ac.uk/calib; accessed December 2016).

1076 Sultan, N., Cochonat, P., Foucher, J. P., Mienert, J., Haflidason, H., Sejrup, H. P. 2003. Effect
1077 of gas hydrates dissociation on seafloor slope stability. In: Locat, J., Mienert, J. (Eds.),
1078 Submarine mass movements and their consequences, Kluwer Academic Publishers, pp.
1079 103–111.

1080 Sultan, N., Cochonat, P., Canals, M., Cattaneo, A., Dennielou, B., Haflidason, H., Laberg,
1081 J.S., Long, D., Mienert, J., Trincardi, F., Urgeles, R., Vorren, T.O., Wilson, C., 2004a.
1082 Triggering mechanisms of slope instability processes and sediment failures on continental
1083 margins: a geotechnical approach. Marine Geology 213, 291–321.

1084 Sultan, N., Cochonat, P., Cayocca, F., Bourilet, J-F., Colliat, J-L., 2004b. Analysis of
1085 submarine slumping in the Gabon continental slope. American Association of Petroleum
1086 Geologists 88, 781–799.

1087 Sultan, N., Cochonat, P., Foucher, J.-P., Mienert, J., 2004c. Effect of gas hydrates melting on
1088 seafloor slope instability. Marine Geology 213, 379–401.

1089 Symonds, P. A., Davies, P. J., Parisi, A., 1983. Structure and stratigraphy of the central Great
1090 Barrier Reef. Bureau Mineral Resoources, Journal of Australian Geology and Geophysics
1091 8, 277–291.

1092 Synolakis, C.E., Bardet, J-P., Borrero, J.C., Davies, H.L., Okal, E.A., Silver, E.A., Sweet, S.,
1093 Tappin, D.R., 2002. The slump origin of the 1998 Papua New Guinea Tsunami.
1094 Proceedings of the Royal Society, London 458, 763–789.

1095 Tappin, D.R., Watts, P., McMurtry, G.M., Lafoy, Y., Matsumoto, T., 2001. The Sissano,
1096 Papua New Guinea tsunami of July 1998 – evidence on the source mechanism. Marine
1097 Geology 175, 1–23.

1098 Tappin, D.R., McNeil, L.C.,Henstock, T.,Mosher, D.C., 2007. Mass wasting processes –
1099 offshore Sumatra. In: Lykousis, V., Sakellariou, D., Locat, J. (Eds.), Submarine mass
1100 movements and their consequences: Advances in natural and technological hazards
1101 research. Springer, pp. 327–337.

Ten Brink, U.S., Geist, E.L., Andrews, B.D., 2006. Size and distribution of submarine landslides and its implications to tsunami hazard in Puerto Rico. Geophysical Research Letters 33, L11307, doi:10.1029/2006GL026125, 2006

Tilbrook, B., Matear, R., 2009. Carbon Chemistry of the Great Barrier Reef. In: CSIRO (Ed), CSIRO Marine National Facility, Hobart, Australia, p. 17.

Todorovska, M.I., Hayir, A., Trifunac, M.D., 2002. A note on tsunami amplitudes above submarine slides and slumps. Soil Dynamics and Earthquake Engineering 22, 129–141.

Tournadour, E., Mulder, T., Borgomano, J., Hanquiez, V., Ducassou, E., Gillet, H., 2015. Origin and architecture of a Mass Transport Complex on the northwest slope of Little Bahama Bank (Bahamas): Relations between off-bank transport, bottom current sedimentation and submarine landslides. Sedimentary Geology 317, 9–26.

Trifunac, M.D., Hayir, A., Todorovska, M.I., 2002. A note on the effects of nonuniform spreading velocity of submarine slumps and slides on the near-field tsunami amplitudes. Soil Dynamics and Earthquake Engineering 22, 167–180.

Twichell, D.C., Chaytor, J.D., ten Brink, U.S., Buczkowski, B., 2009. Morphology of late Quaternary submarine landslides along the U.S. Atlantic continental margin. Marine Geology 264, 4–15.

Urgeles, R., Leynaud, D., Lastras, G., Canals, M., Mienert, J., 2006. Back-analysis and failure mechanisms of a large submarine slide on the Ebro slope, NW Mediterranean. Marine Geology 226, 185–206.

Urlaub, M., Talling, P.J., Masson, D.G., 2013. Timing and frequency of large submarine landslides: implications for understanding triggers and future geohazard. Quaternary Science Reviews 72, 63–82.

Vanneste, M., Mienert, J., Bünz, S., 2006. The Hinlopen Slide: A giant, submarine slope failure on the north Svalbard margin, Artic Ocean. Earth and Platenary Science Letters 245, 373–388.

Viana, A.R., Faugeres, J.C., Kowsmann, R.O., Lima, J.A.M., Caddah, L.F.G., Rizzo, J.G., 1998. Hydrology, morphology and sedimentology of the Campos continental margin, offshore Brazil. Sedimentary Geology 115, 133–157.

Völker, D., Scholz, F., Geersen, J., 2011. Analysis of submarine landsliding in the rupture area of the 27 February 2010 Maule earthquake, Central Chile. Marine Geology 288, 79–89.

Von Huene, R., Ranero, C.R., Watts, P, 2004. Tsunamigenic slope failure along the middle America trench in two tectonic settings. Marine Geology 203, 303–317.

Watts, K.F., Varga, L.L., Feary, D.A., 1993. Origins, timing, and implications of Miocene to Pleistocene turbidites, debris flows, and slump deposits of the Queensland Trough,

northeastern Australia (Site 823). In: McKenzie, J.A., Davies, P.J., Palmer-Julson, A., Sarg, J.F. (Eds), Proceedings of the Ocean Drilling Program, Scientific Results, Vol. 133. Ocean Drilling Program, College Station, Texas, U.S.A., pp. 379–445.

Webster, J.M., Davies, P. J., 2003. Coral variation in two deep drill cores: significance for the Pleistocene development of the Great Barrier Reef. Sedimentary Geology 159, 61–80.

Webster, J.M., Davies, P.J., Beaman, R.J., Williams, S., Byrne, M., 2008. Evolution of drowned shelf edge reefs in the GBR: Implications for understanding abrupt climate change, coral reef response and modern deep water benthic habitats. In: CSIRO (Ed), CSIRO Marine National Facility, Hobart, Australia, p. 18.

Webster, J.M., George, N.P.J., Beaman, R.J., Hill, J., Puga-Bernabéu, Á., Hinestrosa, G., Abbey, E.A., Daniell, J., 2016. Submarine landslides on the Great Barrier Reef shelf edge and upper slope: a mechanism for generating tsunamis on the north-east Australian coast? Marine Geology 371, 120–129.

Weisler, M.I., Hua, Q., Zhao, J., 2009. Late Holocene ^{14}C marine reservoir corrections for Hawai'I derived from U-series dated archaeological coral. Radiocarbon 51, 955–968.

Wiemer, G., Kopf, A., 2015. Altered marine tephra deposits as potential slope failure planes? Geo-Marine Letters 35, 305–314.

Wheeler, A.J., Kozachenko, M., Henry, L.A., Foubert, A., de Haas, H., Huvenne, V.A.I., Masson, D.G., Olu, K., 2011. The Moira Mounds, small cold-water coral banks in the Porcupine Seabight, NE Atlantic: Part A-an early stage growth phase for future coral carbonate mounds? Marine Geology 282, 53–64.

Wolinsky, M.A., Pratson, L.F., 2007. Overpressure and slope stability in prograding clinoforms: Implications for marine morphodynamics. Journal of Geophysical Research 112, F04011, doi:10.1029/2007JF000770.

Figure captions

Figure 1. (A) Bathymetry 30 m DEM of the central part of the north-eastern Australia margin showing the location of the study area (yellow box inset) and main physiographic regions: Great Barrier Reef shelf and Queensland Trough. The slope is excavated by the Noggin Canyon system (Puga-Bernabéu et al., 2013b) and shows a large km-scale shelf indentation at the location of the Gloria Knolls Slide. Blue dots mark the position of the drilling sites of the Ocean Drilling Program Leg 133. Yellow dots mark the location of cores collected on RV *Franklin* Cruise FR4/92. Bathymetry contours in m. (B) Westerly view showing the Gloria Knolls Slide (GKS) and adjacent seafloor features. The GKS is divided into a source area at

1172 the slope (white dashed line) and a depositional area in the trough (pink dashed line). Yellow
1173 lines mark the location of sub-bottom seismic profiles shown in Fig. 5.
1174
1175 **Figure 2. (**A) Bathymetry 30 DEM of the study area showing the three main seafloor terrains
1176 that can be distinguished in the Gloria Knolls Slide based on seafloor morphology: the source
1177 area (SA), the proximal depositional area (PDA) and distal depositional area (DDA).
1178 Headwall scarps (hs) are marked with dashed lines. White lines with letters and black lines
1179 with numbers correspond to depth profiles shown in Fig. 3. (B) Slope gradient map. (C)
1180 Maximum slope direction (aspect). (D) Plan curvature map. (E) Profile curvature map. (F)
1181 Interpreted seafloor features.
1182
1183 **Figure 3.** Depth profiles (see Fig. 2A for location) corresponding to the reconstructed slope
1184 before the Gloria Knoll Slide (black) and present day slope (colour). h and h' indicate the
1185 range of maximum thickness of the slide mass.
1186
1187 **Figure 4.** Westerly view of the distal depositional area of the Gloria Knolls Slide complex
1188 showing the distribution of larger knolls and smaller debris blocks on the seafloor. The knolls
1189 are numbered from 1 to 8. Red numbers mark the location of the two depth profiles shown
1190 across knoll No. 1 and the smaller debris field. Note the presence of moats at the northern
1191 sides of the knolls. White star marks the position of the collected rock dredge on top of knoll
1192 No. 1.
1193
1194 **Figure 5.** TOPAS seismic sections over the depositional area of the Gloria Knolls Slide
1195 (GKS) complex (see Fig. 1B for location). Vertical scale is based on a sound velocity of 1550
1196 m s^{-1} (Davies et al., 1991a). (A) Across profile (main reflectors marked in colours) showing
1197 the sub-bottom character of the GKS deposit characterized by weak amplitude, transparent
1198 reflectors in the proximal depositional area (PDA), and more discontinuous and chaotic in the
1199 distal depositional area (DDA), where pressure-ridges are observed. The basal slide surface is
1200 not observed but notice the presence of blocks rising from deep positions. The GKS deposit is
1201 covered by a drape of hemipelagic sediment and alternating sediment gravity flow deposits
1202 (SGF) (continuous parallel to sub-parallel high amplitude reflectors bundled with low
1203 amplitude reflectors). A small-scale mass-transport deposit occurs close to the GKS headwall
1204 scarp. (B) Along profile (main reflectors marked in colours) showing the sub-bottom
1205 character of the GKS deposit. It includes two mass-transport deposits (M1 and M2)

characterized by transparent reflectors. Note the presence of buried blocks rising from deep position, likely from the basal shear surface. The GKS deposits are covered by a drape of hemipelagic sediment and alternating sediment gravity flow deposits (C). Seismic line over knoll Nos. 1, 3, 7 and 8 and a buried block. Knolls are acoustically opaque and are draped with an up to 15 m thick hemipelagic sediment drape. Note the present of moats at the northern sides of the knolls.

Figure 6. Model of inception and evolution of the Gloria Knolls Slide (GKS) complex slope failure based on seafloor geomorphological analysis and sub-bottom seismic profiles (see text for details). Profiles to the right correspond to cross-section along dashed red line in the left-side drawings. Slope destabilization at water depths of the modern secondary headwall scarp generated the first failure event which left on the seafloor coherent blocks and disintegrated material, which were progressively covered with hemipelagic sediments. Subsequent failure events 2+3 removed significant areas of the slope and formed the main headwall scarp. Failed material in these two events progressively covered the seafloor irregularities and was compressed downslope forming pressure ridges. GKS scarps were subsequently re-shaped by gullies and canyons. More recent slope failures occur after the GKS, likely related to the gully upslope erosion. M1, M2 = mass-transport deposits. SGF = sediment gravity flow.

Supplementary Figure 1. Representative selection of fossil biota and lithified nodules taken from the dredge sample at top of knoll No. 1. Hand lens for scale is 8 cm long. See Figs. 1B and 4 for the dredge location.

Supplementary Material 1. Supplementary methods for U-Th dating.

Supplementary Material 2. Polyline shapefile showing 10 m contour interval multibeam bathymetry over the Gloria Knolls.

Figure 1
Click here to download high resolution image

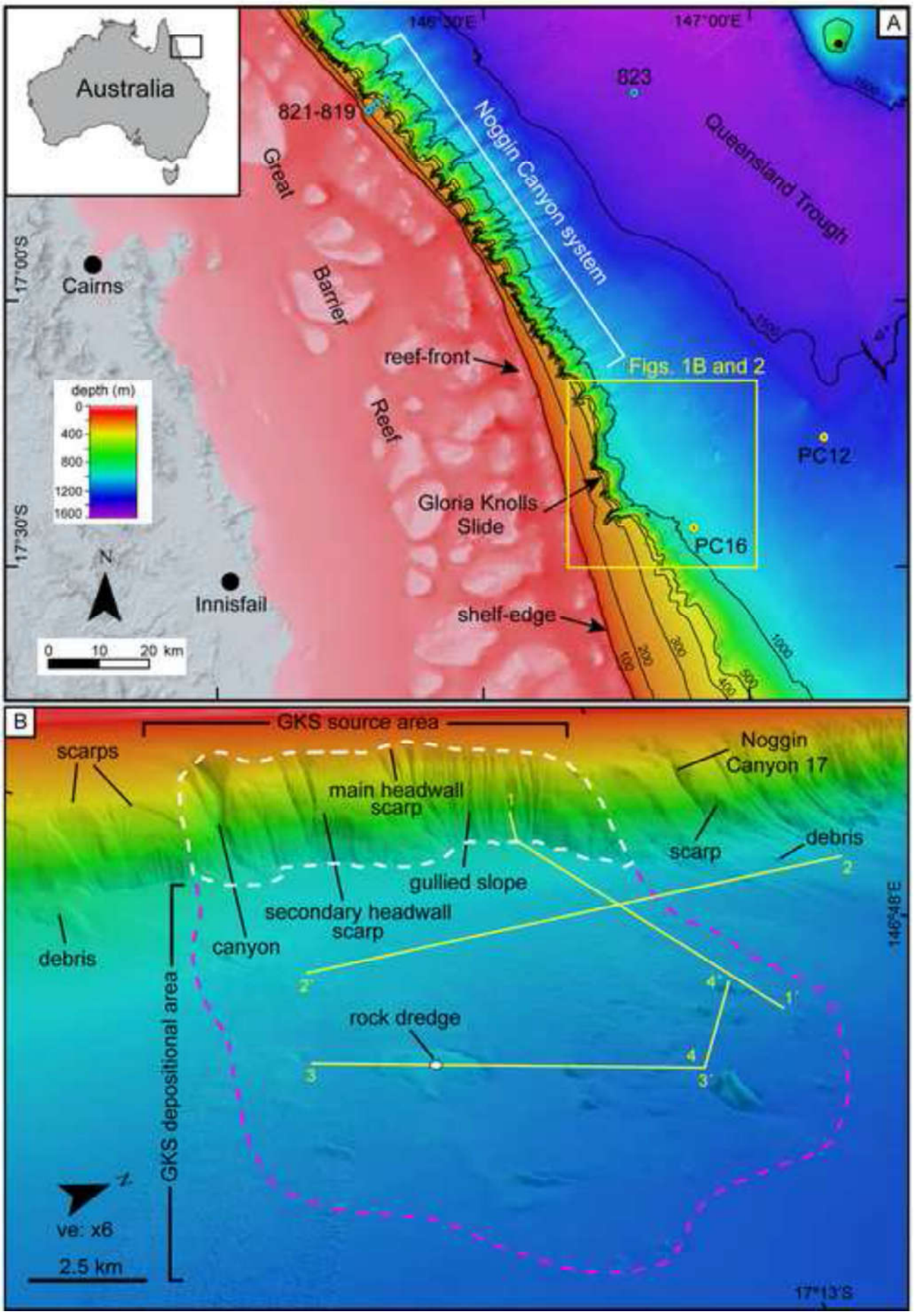

Figure 2
Click here to download high resolution image

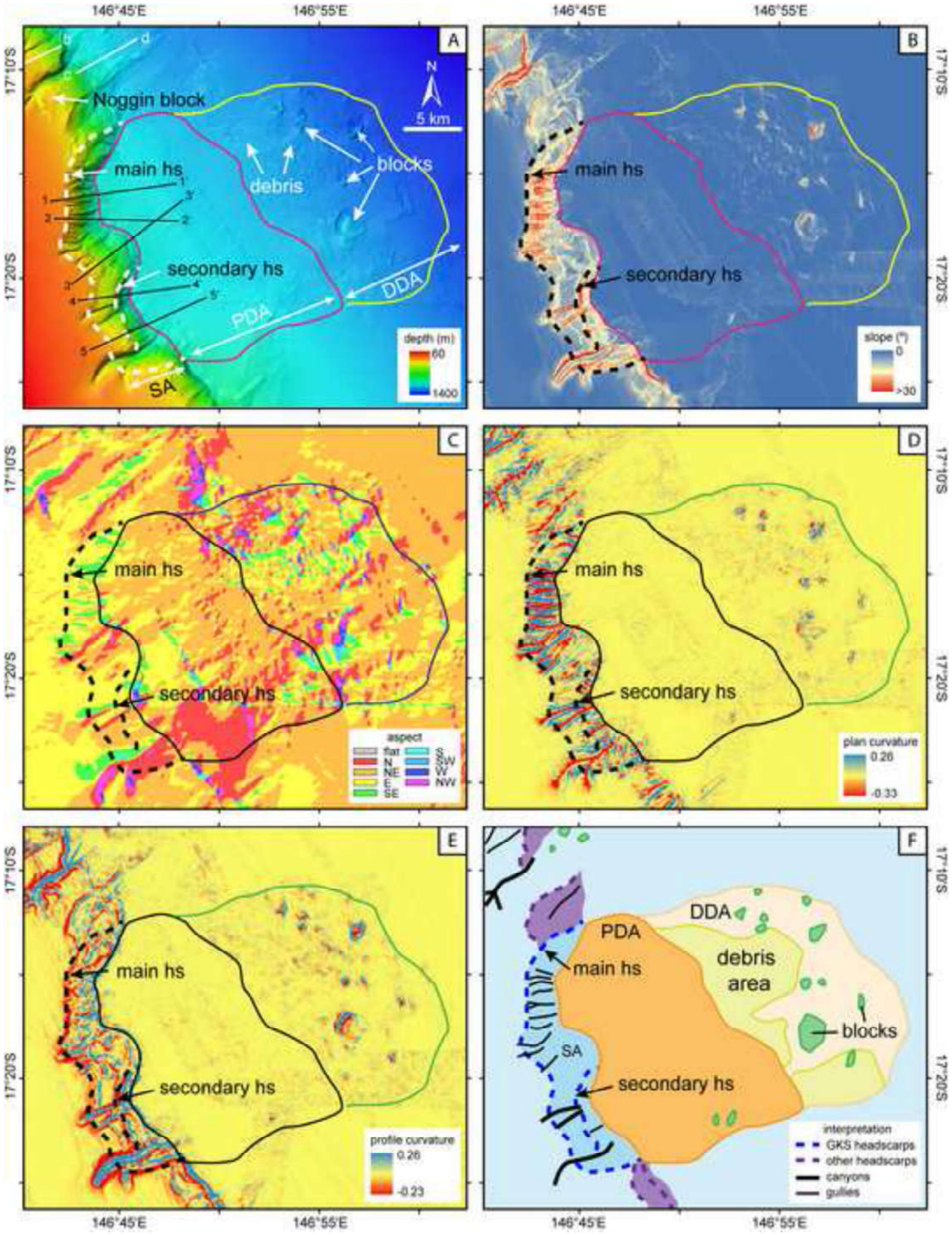

Figure 3

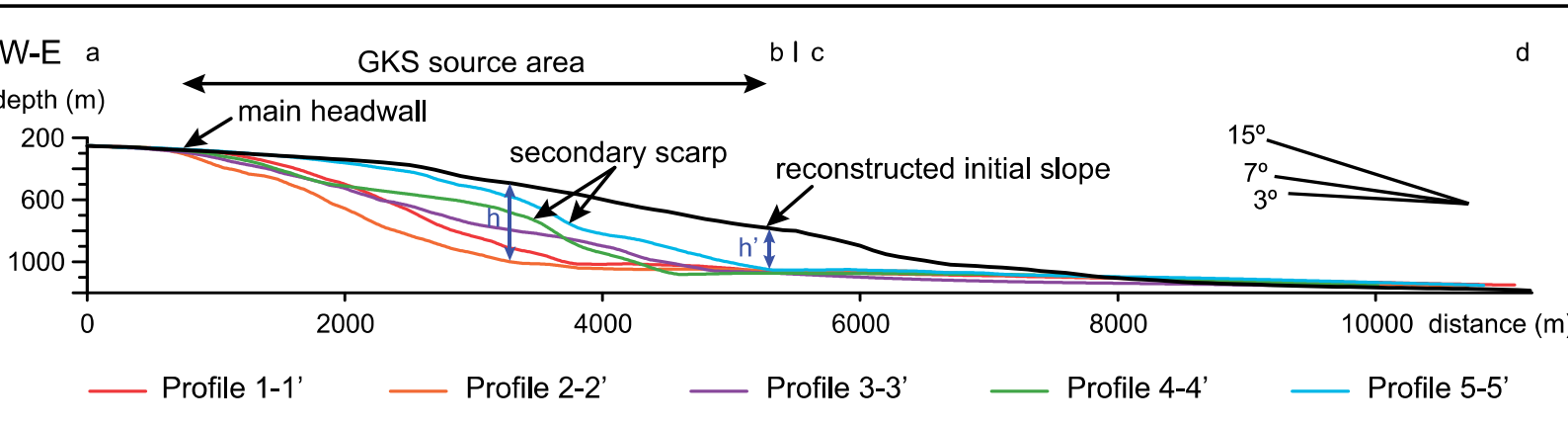
W-E
a
b l c
d
GKS source area
depth (m)
main headwall
secondary scarp
reconstructed initial slope
15°
7°
3°
h
h'
200
600
1000
0
2000
4000
6000
8000
10000
distance (m)
Profile 1-1'
Profile 2-2'
Profile 3-3'
Profile 4-4'
Profile 5-5'

Figure 4

Click here to download high resolution image

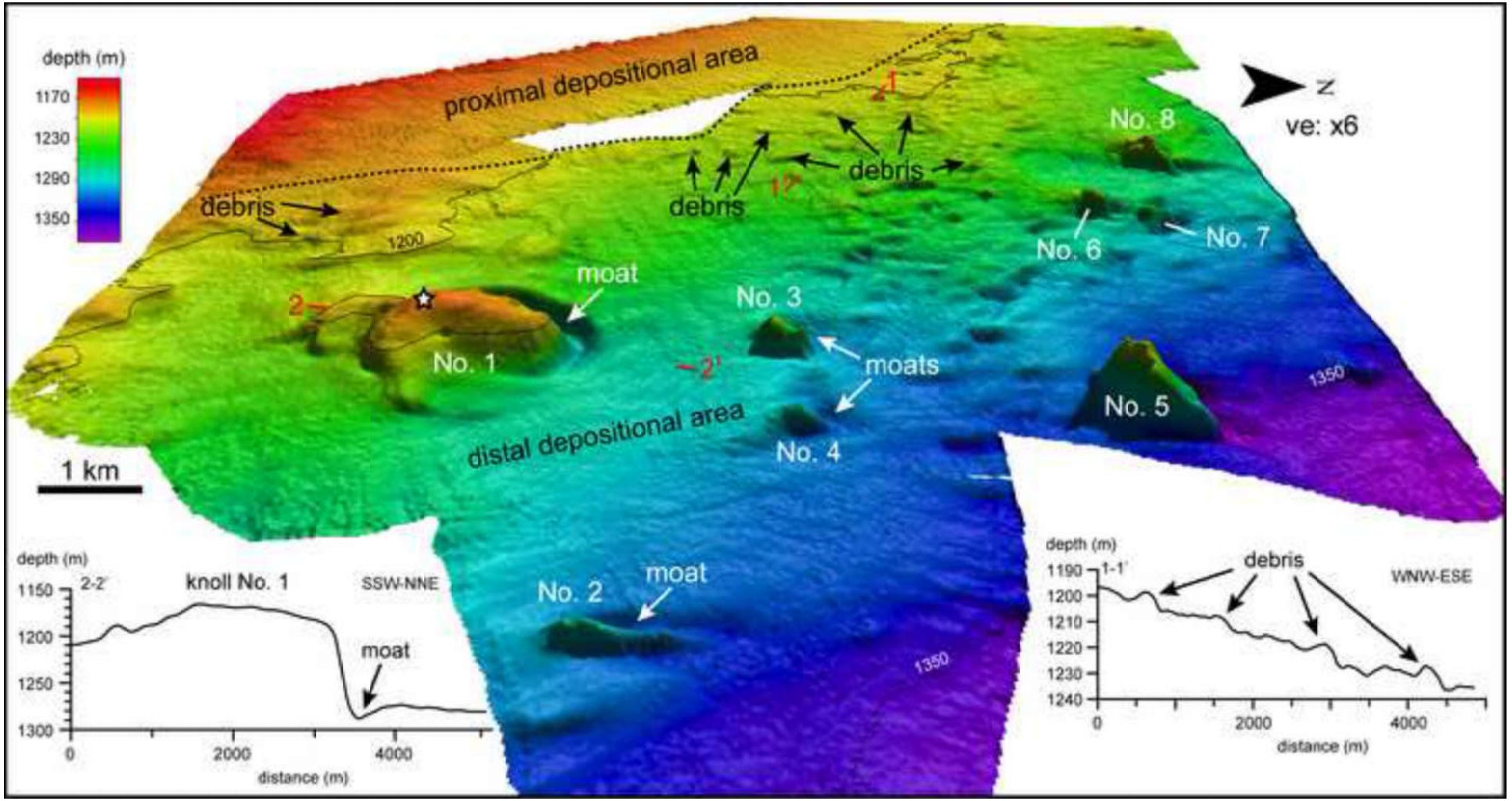

Figure 5
Click here to download high resolution image

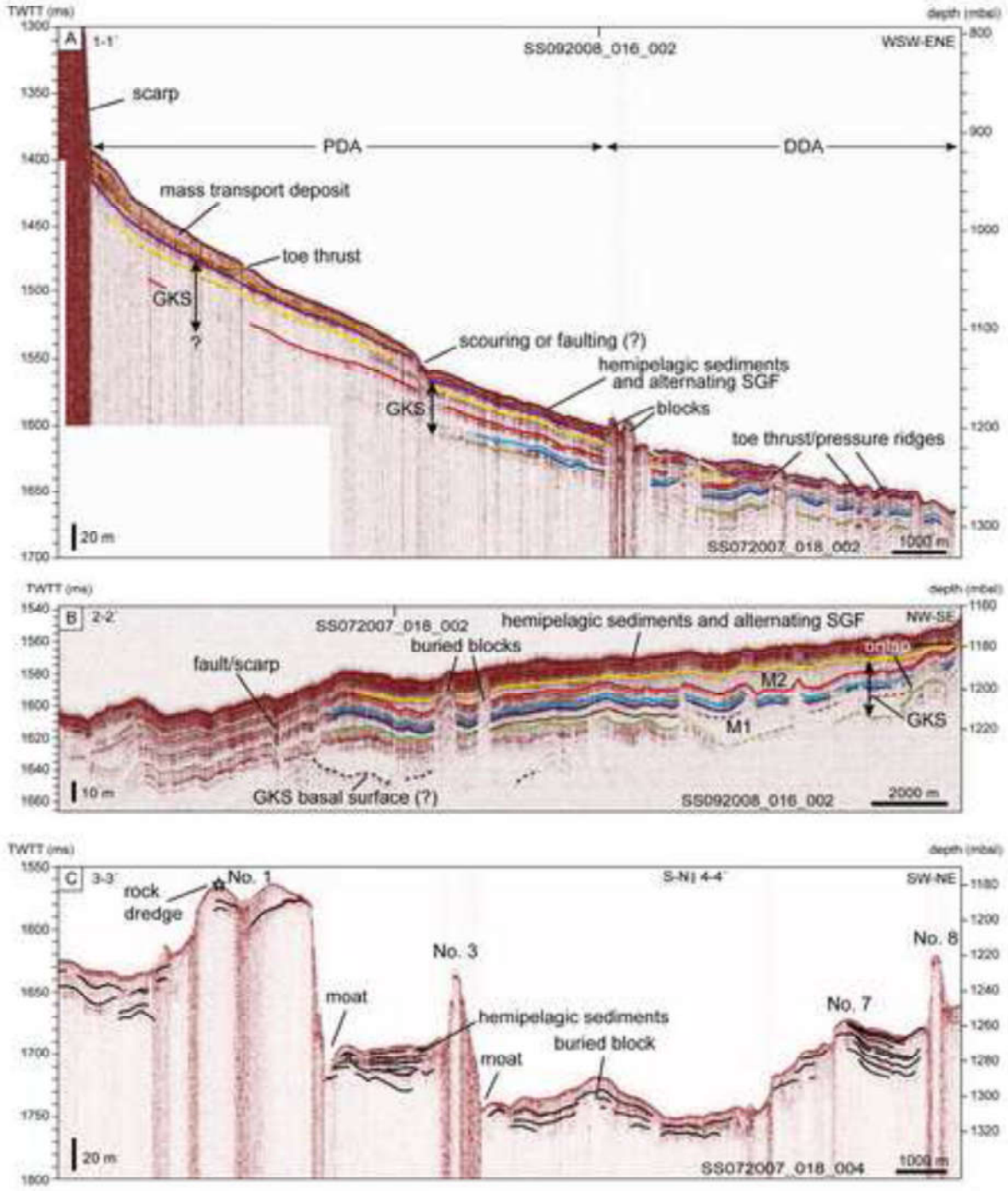

Figure 6

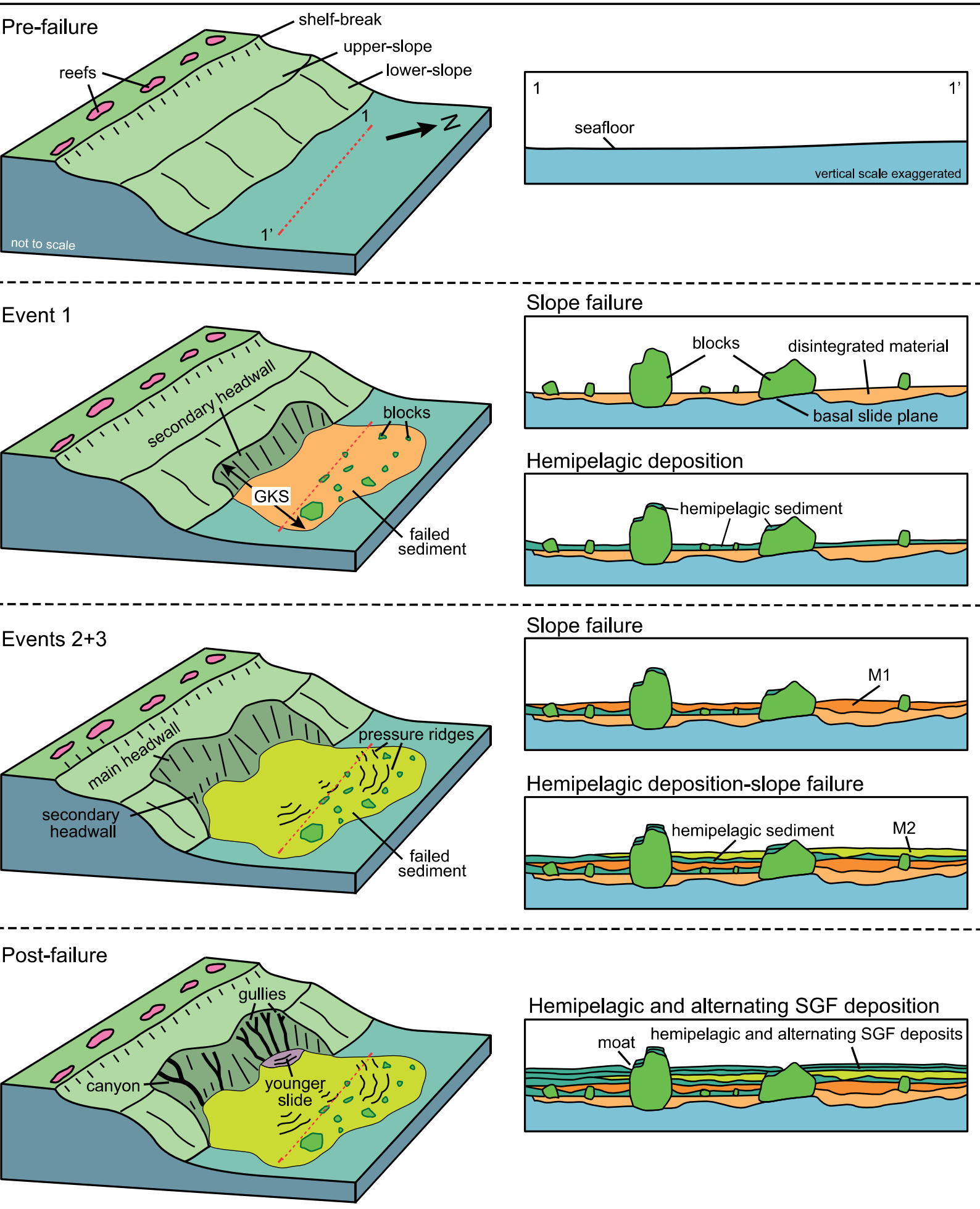
Pre-failure
shelf-break
upper-slope
lower-slope
reefs
1
1'
N
not to scale
1
1'
seafloor
vertical scale exaggerated
Event 1
secondary headwall
blocks
GKS
failed sediment
Slope failure
blocks
disintegrated material
basal slide plane
Hemipelagic deposition
hemipelagic sediment
Events 2+3
main headwall
pressure ridges
secondary headwall
failed sediment
Slope failure
M1
Hemipelagic deposition-slope failure
hemipelagic sediment
M2
Post-failure
gullies
canyon
younger slide
Hemipelagic and alternating SGF deposition
moat
hemipelagic and alternating SGF deposits

Table 1. Parameters of the Gloria Knolls Slide complex.

Length (km): ~31
Width (km): ~ 20
Across slope source area width (km): ~ 8
Area (km^2): ~528
Area of slope removed ((km^2): ~174
Volume (km^3): ~32
Water depth source area (mbsl): 250 to 1050
Water depth deposition area (mbsl): ~1050 to 1350
Headwall height (m): 670 to 830
Headwall scarp gradient: 15º (average)
Unfailed adjacent slope gradient: 6-7º (average)
Estimated thickness of failed section (m): 260 to 500
Estimated thickness of the deposits (m): 17 to 37

Table 2
Click here to download Table: Table 2.docx

Table 2. Positions and dimensions of the Gloria Knolls within the distal depositional area (see Figs. 2 and 4).

No.	Latitude (South)	Longitude (East)	Max. length (km)	Min. width (km)	Area (km^2)	Min. depth (m)	Max. depth (m)	Height (m)
1	17°17.87'	146°56.30'	3.6	1.5	7.9	1165	1270	105
2	17°16.53'	146°59.08'	1.6	0.4	1.2	1268	1312	44
3	17°15.52'	146°56.29'	0.9	0.7	0.7	1226	1309	83
4	17°15.39'	146°57.16'	0.9	0.5	0.5	1265	1328	63
5	17°13.20'	146°56.75'	1.9	1.3	2.1	1196	1375	179
6	17°12.80'	146°54.13'	0.7	0.5	0.6	1215	1280	65
7	17°12.35'	146°54.23'	0.9	0.6	0.8	1245	1316	71
8	17°12.05'	146°53.01'	1.2	0.8	1.5	1189	1258	69

Table 3

Click here to download Table: Table 3.docx

Table 3. Sediment sample analysis for CNS, size classes and XRD results.

Sample type	Nitrogen weight %	Carbon weight %	Sulfur weight %	$CaCO_3$ weight %	Mud vol %	Sand vol %	Gravel vol %	Carbonates weight %	Quartz weight %	Clays weight %
soft mud	0.03	6.56	0.04	54.67	59.62	40.38	0.00	82.2	7.9	10.0
semi-lithified nodule	0.03	9.34	0.03	77.87	67.52	32.48	0.00	78.1	8.4	13.6
lithified nodule	0.02	10.55	0.03	87.92	NA	NA	NA	83.5	8.6	7.8

Table 4

Table 4. AMS and U-Th ages from fossil samples recovered from the Gloria Knoll No. 1 at 1170 m water depth (see Figs. 1B and 4 for location).

ANSTO lab code	Sample code	Sample name	Radiocarbon age kyr BP	1σ error kyr	Calibrated age cal kyr BP (2σ)	Calibrated Age cal kyr BP (2σ)	U-Th age yr BP	2σ error yr
OZL546	bamboo coral 1	unknown sp.	19.10	0.09	21.34±0.37	20.98-21.71		
OZL547	scleractinian coral 1	*Enallopsammia* sp.	51.90	1.10	Not calibrated	Not calibrated	301,899	19,105
OZL548	scleractinian coral 2	*Enallopsammia rostrata*	2.56	0.04	1.07±0.16	0.91-1.23	1,066	34
OZL549	scleractinian coral 3	*Madrepora oculata*	2.28	0.04	0.78±0.14	0.65-0.93	914	306
OZL550	gastropod 1	*Calliotropis pagodiformis*	26.83	0.16	29.47±0.52	28.95-29.99		
OZL551	gastropod 2	*Pontiothauma* sp.	5.40	0.05	4.52±0.26	4.26-4.78		
OZL552	coral on semi-lith. nodule	unknown sp.	5.08	0.04	4.06±0.23	3.82-4.29		
OZL553	coral on lith. nodule	unknown sp.	8.59	0.05	8.00±0.18	7.82-8.18		
OZL554	lithified nodule		44.78	0.64	46.66±1.34	45.32-48.01		
OZL555	barnacle 1	*Scillaelepas fosteri*	3.25	0.04	1.79±0.19	1.59-1.98		
OZL556	barnacle 2	*Scillaelepas fosteri*	2.54	0.04	1.06±0.16	0.89-1.23		
OZL557	pteropod	*Cavolinia tridentata*	3.66	0.05	2.29±0.23	2.06-2.52		
OZL558	bamboo coral 2	unknown sp.	2.78	0.04	1.30±0.18	1.12-1.48		

Calibrated against the Marine13 calibration curve (Reimer et al., 2013) using CALIB7.1 (Stuiver et al., 2005), with an estimated ΔR= 1,045±75 ^{14}C yrs BP

Supplementary Figurel 1

Click here to download Supplementary Materials: Supplementary Figure 1.tif

Supplementary Material 2

Click here to download Supplementary Materials: GloriaKnolls_contour10m.dbf

Supplementary Material 1

Click here to download Supplementary Materials: Supplementary Material 1.docx

Supplementary Material 2

Click here to download Supplementary Materials: GloriaKnolls_contour10m.prj

Supplementary Material 2

Click here to download Supplementary Materials: GloriaKnolls_contour10m.sbn

Supplementary Material 2

Click here to download Supplementary Materials: GloriaKnolls_contour10m.sbx

Supplementary Material 2

Click here to download Supplementary Materials: GloriaKnolls_contour10m.shp

Supplementary Material 2

Click here to download Supplementary Materials: GloriaKnolls_contour10m.shp.xml

Supplementary Material 2

Click here to download Supplementary Materials: GloriaKnolls_contour10m.shx